O.V. Lounasmaa Laboratory

Decoherence in Superconducting Quantum Circuits

Jian Li

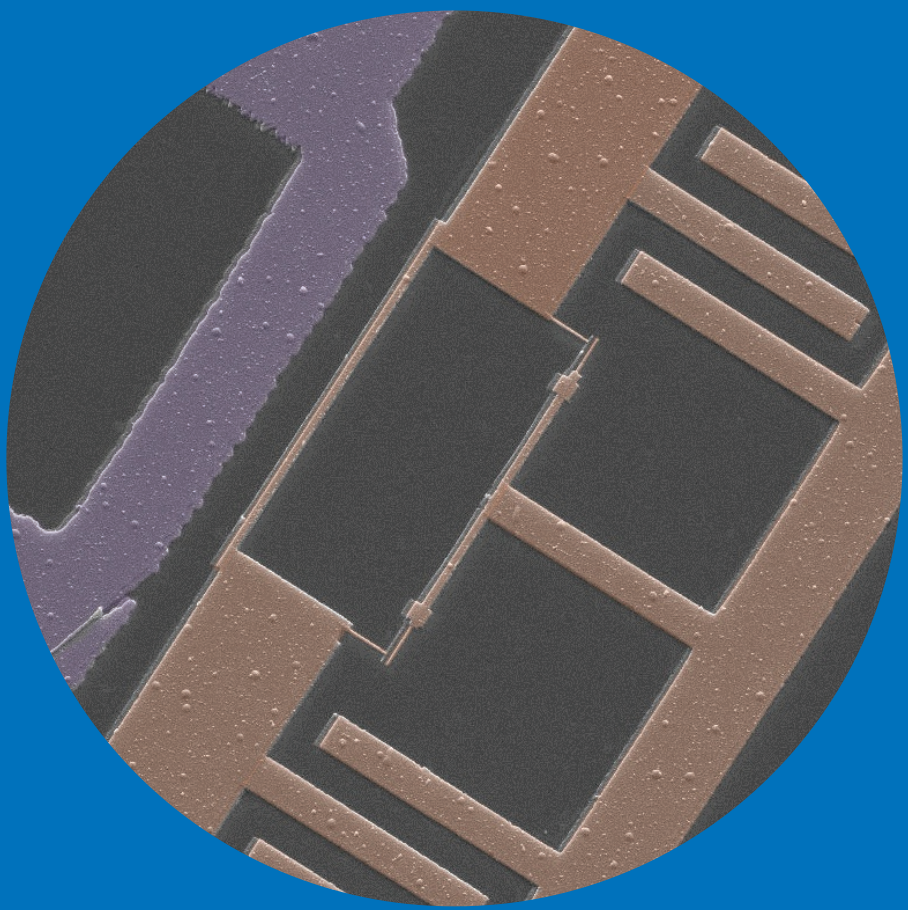

Aalto University

DOCTORAL DISSERTATIONS

Aalto University publication series
DOCTORAL DISSERTATIONS 102/2012

Decoherence in Superconducting Quantum Circuits

Jian Li

Doctoral dissertation for the degree of Doctor of Science in Technology to be presented with due permission of the School of Science for public examination and debate in Auditorium F239a at the Aalto University School of Science (Espoo, Finland) on the 24th of August 2012 at 12 noon.

Aalto University
School of Science
O.V. Lounasmaa Laboratory
Kvantti Group

Supervising professor
Prof. Matti Kaivola

Thesis advisor
Dr. Sorin Paraoanu

Preliminary examiners
Prof. Yuriy Makhlin, Landau Institute for Theoretical Physics, Russia
Dr. Sahel Ashhab, RIKEN, Japan

Opponent
Assist. Prof. Leonardo DiCarlo, Delft University of Technology, The Netherlands

Aalto University publication series
DOCTORAL DISSERTATIONS 102/2012

ISBN 978-952-60-4729-4 (printed)
ISBN 978-952-60-4730-0 (pdf)
ISSN-L 1799-4934
ISSN 1799-4934 (printed)
ISSN 1799-4942 (pdf)
http://urn.fi/URN:ISBN:978-952-60-4730-0

Unigrafia Oy
Helsinki 2012

Finland

Author
Jian Li

Name of the doctoral dissertation
Decoherence in Superconducting Quantum Circuits

Publisher School of Science

Unit O.V. Lounasmaa Laboratory

Series Aalto University publication series DOCTORAL DISSERTATIONS 102/2012

Field of research Engineering Physics, Quantum Information

Manuscript submitted 4 April 2012 **Date of the defence** 24 August 2012

Permission to publish granted (date) 7 June 2012 **Language** English

☐ **Monograph** ☒ **Article dissertation (summary + original articles)**

Abstract

Superconducting quantum devices have drawn the attention of physicists greatly in recent years, not only because they are one of the most favorable candidates for developing a solid state quantum computer, but also because they can be employed as test systems for understanding quantum mechanics at nearly macro scale. Superconducting quantum devices can be divided into two groups: the superconducting resonators (linear devices), which have equally spaced discrete energy levels, and the artificial atoms (non-linear devices) consisting of Josephson junctions which have unequally spaced discrete energy levels. By combining these two kinds of devices together, a solid state counterpart of optical cavity quantum electrodynamics (QED) known as circuit QED emerges. Experiments of cavity QED and quantum optics can be reproduced in either circuit QED systems or in bare superconducting artificial atoms. As an example, we have observed the Autler-Townes effect in a three-level artificial atom called phase qutrit.

More than one decade has passed since the first experimental demonstration of superconducting two-level artificial atom (qubit). However, to build a practical quantum computer with thousands of superconducting qubits there is still a long way to go (we are at the stage of three qubits now). One of the main obstacles preventing us from scaling up a superconducting quantum computer, as well as some other kinds of quantum computers, has been decoherence, which is believed to be dominated by the low frequency noise due to the two-level system (TLS) fluctuators located inside the Josephson junction barrier. We have experimentally simulated the dynamics of a qubit longitudinally coupled to a randomly fluctuating TLS. A phenomenon known as motional averaging has been observed.

In this thesis, theoretical models for decoherence in both resonator and artificial atoms have been established and used for explaining phenomena observed in the experiments performed in our laboratory. The phenomenon of decoherence in coupled bipartite systems has been also studied, and besides the already known entanglement sudden death phenomenon, stable entanglement (robust under decoherence) generated from an arbitrary initial state has been found in these systems.

Keywords Superconducting artificial atoms, circuit QED, decoherence, TLS, Autler-Townes effect, motional averaging, entanglement sudden death

ISBN (printed) 978-952-60-4729-4 **ISBN (pdf)** 978-952-60-4730-0

ISSN-L 1799-4934 **ISSN (printed)** 1799-4934 **ISSN (pdf)** 1799-4942

Location of publisher Espoo **Location of printing** Helsinki **Year** 2012

Pages 196 **urn** http://urn.fi/URN:ISBN:978-952-60-4730-0

Preface

The research work presented in this thesis was mainly carried out at the O.V. Lounasmaa Laboratory of Aalto University between early 2008 and early 2012. Some early calculations were done at the Nanoscience Center of University of Jyväskylä between late 2006 and late 2007.

First and foremost, I would like to thank my supervisor, as well as the leader of the Kvantti group, Docent Sorin Paraoanu very much from the bottom of my heart, for introducing me into the field of superconducting quantum circuits, for the instructive guidance and ideas throughout my studies and researches, and for all kinds of help he has given to me since 2006.

Second, I would like to thank Khattiya Chalapat, a member of the Kvantti group who also moved from University of Jyväskylä to Aalto University, for such a long time cordial working relationship, and for our friendship.

Then many thanks to Assoc. Prof. Mika Sillanpää for helping me with learning practical low temperature measurement techniques and with operating dilution refrigerators, and especially for offering me a PostDoc position in his group. Many thanks also to Dr. Alexander Savin for his patience and valuable advices to help me solve problems in cooling downs, especially at the early stage of my measurements.

I am so grateful to Prof. Pertti Hakonen, the director of the O.V. Lounasmaa Laboratory and the leader of the Nano group, for enlightening discussions, for constructive suggestions for the manuscripts, and for the help with my PostDoc applications.

It has been a great privilege to work with all the present members and alumni in the Kvantti group and with our collaborators from the NEMS group: Karthikeyan Kumar, Robab Jabdaraghi, Antti Vepsäläinen, Joonas Govenius, Jaakko Sulkko, Juha-Matti Pirkkalainen, Sung Un Cho, Maria Berdova and Meri Helle.

I am grateful to all the colleagues who used to be and presently are in Office

Room 162a: Vitaly Emets, Pasi Häkkinen, Raphaël Khan, Matti Laakso, Dmitry Lyashenko, Pasi Lähteenmäki, Mika Oksanen, Antti Puska, Antti Paila, Jayanta Sarkar, Xuefeng Song, Matti Tomi, Aurélien Fay, Fan Wu, Romain Danneau and Juha Voutilainen, for their efforts to create a pleasant and lively working atmosphere. I am also grateful to Prof. Erkki Thuneberg, Dr. Tero Heikkilä, Dr. Francesco Massel, Prof. Jukka Pekola, Prof. Mikko Paalanen, and the secretaries of the O.V. Lounasmaa Laboratory: Sari Laitila, Teija Halme, Olga Jakkola and Susanna Jauhiainen.

I also thank our collaborators outside the O.V. Lounasmaa Laboratory: Katarina Cicak, Fabio Altomare, Jae Park and Raymond Simmonds from NIST Boulder, for the valuable communications and discussions. Special thanks to Dr. David Gunnarsson from VTT for the samples and enjoyable discussions, and to Matti Silveri from University of Oulu who has been working on our current project so hard.

Discussions with Prof. John Martinis, Prof. Steven Girvin, Prof. Yuriy Makhlin and Prof. Jaw-Shen Tsai are gratefully acknowledged. The financial supports of my studies from the Academy of Finland under a grant of my supervisor Sorin Paraoanu and from National Graduate School in Materials Physics (NGSMP) are also acknowledged.

I am deeply grateful to my parents for their endless supports and encouragements. Last but not least, I thank all of my friends in Helsinki region and in Jyväskylä.

Espoo, July 23, 2012,

Jian Li

Contents

List of Publications

This thesis consists of an overview and of the following publications which are referred to in the text by their Roman numerals.

I Jian Li, K. Chalapat, and G. S. Paraoanu. Entanglement of superconducting qubits via microwave fields: Classical and quantum regimes. *Physical Review B*, **78**, 064503, August 2008.

II Jian Li, K. Chalapat, and G. S. Paraoanu. Enhancement of sudden death of entanglement for driven qubits. *Journal of Low Temperature Physics*, **153**, 294, October 2008.

III Jian Li, K. Chalapat, and G. S. Paraoanu. Measurement-induced entanglement of two superconducting qubits. *Journal of Physics: Conference Series*, **150**, 022051, March 2009.

IV Jian Li and G. S. Paraoanu. Decay of entanglement in coupled, driven systems with bipartite decoherence. *The European Physical Journal D*, **56**, 255, September 2009.

V Jian Li and G. S. Paraoanu. Generation and propagation of entanglement in driven coupled-qubit systems. *New Journal of Physics*, **11**, 113020, November 2009.

VI Mika A. Sillanpää, Jian Li, Katarina Cicak, Fabio Altomare, Jae I. Park, Raymond W. Simmonds, G. S. Paraoanu, and Pertti J. Hakonen. Autler-Townes Ef-

fect in a Superconducting Three-Level System. *Physical Review Letters*, **103**, 193601, November 2009.

VII Jian Li, G. S. Paraoanu, Katarina Cicak, Fabio Altomare, Jae I. Park, Raymond W. Simmonds, Mika A. Sillanpää, and Pertti J. Hakonen. Decoherence, Autler-Townes effect, and dark states in two-tone driving of a three-level superconducting system. *Physical Review B*, **84**, 104527, September 2011.

VIII Jian Li, G. S. Paraoanu, Katarina Cicak, Fabio Altomare, Jae I. Park, Raymond W. Simmonds, Mika A. Sillanpää, and Pertti J. Hakonen. Operation of a phase qubit as a microwave switch. *arXiv*, 1103.2631, March 2011.

IX Jian Li and G. S. Paraoanu. Dynamical decoupling of superconducting qubits. *Journal of Physics: Conference Series*, **338**, 012010, February 2012.

X Jian Li, M. P. Silveri, K. S. Kumar, J.-M. Pirkkalainen, A. Vepsäläinen, W. C. Chien, J. Tuorila, M. A. Sillanpää, P. J. Hakonen, E. V. Thuneberg, and G. S. Paraoanu. Motional Averaging in a Superconducting Qubit. *arXiv*, 1205.0675, May 2012.

Author's Contribution

Publication I: "Entanglement of superconducting qubits via microwave fields: Classical and quantum regimes"

The author did the main analytical calculations and the numerical simulations, and wrote major parts of the manuscript.

Publication II: "Enhancement of sudden death of entanglement for driven qubits"

The author did the main analytical calculations and the numerical simulations, and wrote the manuscript.

Publication III: "Measurement-induced entanglement of two superconducting qubits"

The author did parts of the analytical calculations and the numerical simulations, and wrote parts of the manuscript.

Publication IV: "Decay of entanglement in coupled, driven systems with bipartite decoherence"

The author did the main analytical calculations and the numerical simulations, and wrote major parts of the manuscript.

Publication V: "Generation and propagation of entanglement in driven coupled-qubit systems"

The author did the main analytical calculations and the numerical simulations, and wrote parts of the manuscript.

Publication VI: "Autler-Townes Effect in a Superconducting Three-Level System"

The author developed the theoretical model, performed the numerical simulations, and assisted in the measurements.

Publication VII: "Decoherence, Autler-Townes effect, and dark states in two-tone driving of a three-level superconducting system"

The author did the main analytical calculations and the numerical simulations, and wrote major parts of the manuscript.

Publication VIII: "Operation of a phase qubit as a microwave switch"

The author did the main analytical calculations and the numerical simulations, and wrote parts of the manuscript.

Publication IX: "Dynamical decoupling of superconducting qubits"

The author did the main analytical calculations and the numerical simulations, and wrote major parts of the manuscript.

Publication X: "Motional Averaging in a Superconducting Qubit"

The author had the main responsibility for the measurements and the data analysis, did some of the numerical simulations, and contributed significantly to the writing of the manuscript.

1. Introduction

In the past decade, the field of quantum computation on both the experimental and the theoretical sides, has developed rapidly. A wide range of quantum systems have been studied for their potential of being scalable qubits to implement practical quantum computer. A special group of qubits are based on superconducting circuits containing Josephson junctions. A Josephson junction is formed by connecting two superconducting electrodes via a weak link (a thin layer of insulator or normal metal, *etc.*). In the superconducting electrodes, two electrons with equal and opposite momentum and spin can pair up to form a so-called Cooper pair. At sufficiently low temperature, a large number of Cooper pairs in each superconducting electrode can condense into one quantum state and thus behave as a single quantum particle. When there is a phase difference between the two condensates of Cooper pairs in the two electrodes, a current can flow through the weak link even without any bias voltage applied to the two electrodes. This effect is known as the *dc* Josephson effect [1]. In contrast with other qubit proposals by using microscopic particles such as trapped single atoms or electrons, the superconducting circuits are essentially macroscopic quantum systems. The superconducting circuits are solid state devices fabricated by modern integrated circuits fabrication techniques, and manipulated and measured by well-developed low frequency electronics and microwave techniques. As a result, these systems can in principle be easily scaled up.

The superconducting circuits also show great potential in some other aspects of physics, both practical and fundamental. For instance, the *ac* Josephson effect, which relates frequencies to bias voltages, makes the Josephson junction very important in metrology. The inductance of a *dc* superconducting quantum interference device (SQUID) can be tuned rapidly by applying a *rf* magnetic field through the SQUID loop. This tunability makes superconducting circuits consisting of *dc* SQUIDs promising candidates for observing the dynamic Casimir effect [2, 3].

The macroscopic structure of a superconducting quantum circuit enhances the coupling of the circuit to its environment. The environment induces dynamical destruction of quantum coherence of the circuit, which is known as *decoherence*. Decoherence has been an active research subject since early 1980s [4]. Until early 1990s the theory of decoherence was mainly a solution to the fundamental interpretation problems of quantum mechanics [5]. The effects of decoherence processes on coherent quantum operations were first introduced in 1995 [6, 7]. A general model that describes the environment-induced decoherence process is the Caldeira-Leggett model proposed by Caldeira and Leggett in 1981 [8]. In quantum computation, a more specialized model known as the spin-boson[1] model is commonly used, and quite often the Markov approximation, in which the dynamics of the qubit is assumed to be much slower than the destruction of the environment's correlations, is also applied. The Markov approximation relies on the assumption that the number of modes in the collection of harmonic oscillators is nearly infinite[2]. For superconducting qubits, the spin-boson model and the Markov approximation work fine in most cases. However, when a superconducting qubit is coupled to a few two-level system (TLS) fluctuators, the environment (the TLSs) can be neither bosonic nor Markovian.

This thesis is organized as follows. Chapter 2 introduces the quantum circuit theory by studying a superconducting *LC* resonator, discusses damping of the resonator due to voltage fluctuation, and describes how to experimentally design, fabricate and characterize a superconducting coplanar waveguide resonator. Chapter 3 briefly reviews three designs of superconducting artificial atoms based on Josephson junctions as well as the circuit quantum electrodynamics (QED). Chapter 4 is devoted to the theoretical descriptions of decoherence in the artificial atoms. The Markov master equations for two- and three-level artificial atoms are given in this chapter. The entanglement sudden death, a quantum phenomenon due to decoherence in a bipartite system, is also studied in Chapter 4. Chapter 5 reviews the results from the experiments on the Autler-Townes effect in a superconducting three-level atom. Chapter 6 is devoted to the experiments on the motional averaging in a circuit QED system. A simulation of decoherence caused by a longitudinally coupled two-level system fluctuator is demonstrated. The thesis summary and future prospects are given in the last chapter.

[1] "Spin" and "boson" stand for a qubit (a two-level atom or a spin-$1/2$ particle) and a collection of harmonic oscillators, respectively.

[2] This is the reason why sometimes an environment is also called a reservoir. The term "reservoir" refers to an environment with an infinite number of degrees of freedom [9].

2. Superconducting LC Resonator

Superconducting LC resonators play a vital role in circuit QED systems, just as optical cavities do in conventional quantum optics. Besides, as we will see in the next chapter, understanding the physics of superconducting LC resonators is a key factor for the construction of superconducting artificial atoms. So in this chapter, a voltage driven superconducting LC resonator will be discussed. This chapter begins with a detailed theoretical description of the driven superconducting resonator, then proceeds by studying a specific kind of superconducting resonator from a technical point of view.

2.1 Theoretical point of view

A LC resonator is one of the simplest circuits. It consists of an inductor with inductance L and a capacitor with capacitance C. It is well known that this circuit can behave as a harmonic oscillator. The goal of this section is to derive a quantum Hamiltonian of the LC resonator analogous to that of a mechanical harmonic oscillator [10].

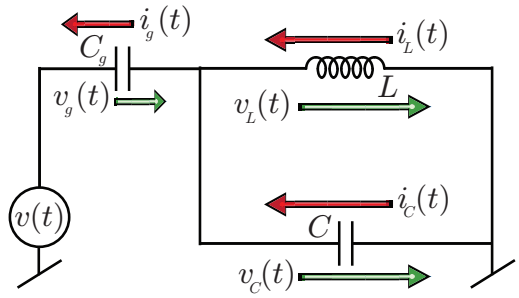

Figure 2.1. A LC circuit couples to a voltage source via a gate capacitor.

In contradistinction with a circuit consisting of only L and C in parallel, here

we consider a slightly more complicated case: the circuit couples to an external voltage source, providing time-varying voltage $v(t)$, via a gate capacitance C_g, as shown in Fig. 2.1. To get rid of resistive dissipations, the whole circuit is assumed to be made of perfect conductors[1].

There are three passive elements in this circuit, and each element at arbitrary time t is characterized by the current (red arrows in Fig. 2.1) flowing through it and the voltage (green arrows in Fig. 2.1) across it [11],

$$v_L(t) = L\frac{di_L(t)}{dt}, \;\; i_C(t) = C\frac{dv_C(t)}{dt} \;\text{ and }\; i_g(t) = C_g\frac{dv_g(t)}{dt}. \tag{2.1}$$

If we take time integrals of both sides of equations above, we obtain

$$i_L(t) = \frac{\Phi_L(t)}{L}, \;\; v_C(t) = \frac{Q_C(t)}{C} \;\text{ and }\; v_g(t) = \frac{Q_g(t)}{C_g}, \tag{2.2}$$

where the so-called branch flux Φ_L, the branch charges Q_C and Q_g [11] are defined as

$$\Phi_L(t) = \int_{-\infty}^{t} d\tau v_L(\tau), \;\; Q_C(t) = \int_{-\infty}^{t} d\tau i_C(\tau) \;\text{ and }\; Q_g(t) = \int_{-\infty}^{t} d\tau i_g(\tau). \tag{2.3}$$

The branch fluxes for the capacitors can also be calculated by $\Phi_C(t) = \int_{-\infty}^{t} d\tau v_C(\tau)$ and $\Phi_g(t) = \int_{-\infty}^{t} d\tau v_g(\tau)$, and the stored (capacitive) energies are

$$E_C = \frac{1}{2}Cv_C^2(t) = \frac{1}{2}C\left[\frac{d\Phi_C(t)}{dt}\right]^2, \quad E_g = \frac{1}{2}C_g v_g^2(t) = \frac{1}{2}C_g\left[\frac{d\Phi_g(t)}{dt}\right]^2. \tag{2.4}$$

The stored (inductive) energy of the inductor is equivalent to the work carried out by an energy source that has provided $v_L(t)$ and $i_L(t)$,

$$E_L = \int_{-\infty}^{t} d\tau v_L(\tau) i_L(\tau) = \frac{1}{2L}\Phi_L^2(t). \tag{2.5}$$

The Lagrangian of the whole circuit is the difference between the capacitive (kinetic) energies and the inductive (potential) energy, $\mathcal{L}_{\rm R} = E_C + E_g - E_L$. By taking the voltage constrains (from Kirchhoff's voltage law),

$$\dot{\Phi}_C(t) = \dot{\Phi}_L(t) \equiv \dot{\Phi}(t) \;\text{ and }\; v(t) + \dot{\Phi}_g(t) + \dot{\Phi}(t) = 0, \tag{2.6}$$

into account, where $\dot{\Phi}_{(C,L,g)}(t) = d\Phi_{(C,L,g)}(t)/dt$, the Lagrangian has the form

$$\mathcal{L}_{\rm R}(t) = \frac{1}{2}C\dot{\Phi}^2(t) + \frac{1}{2}C_g\left[\dot{\Phi}(t) + v(t)\right]^2 - \frac{1}{2L}\Phi^2(t). \tag{2.7}$$

The corresponding Euler-Lagrange equation is

$$C_\Sigma\ddot{\Phi}(t) + \frac{1}{L}\Phi(t) + C_g\dot{v}(t) = 0, \tag{2.8}$$

[1]To keep the discussions in this section simple, I will not introduce the idea of superconductivity, and just assume that the conductors have zero resistance.

describing the motion of a one-dimensional harmonic oscillator driven by a variable force $C_g\dot{v}(t)$ [12]. Here $C_\Sigma = C + C_g$ represents the total capacitance of the circuit.

The Hamiltonian is obtained by performing a Legendre transformation on the Lagrangian,

$$H_{\rm R}(t) = \frac{\partial \mathcal{L}_{\rm R}(t)}{\partial \dot{\Phi}(t)}\dot{\Phi}(t) - \mathcal{L}_{\rm R}(t) = \frac{1}{2C_\Sigma}\left[Q(t) - C_g v(t)\right]^2 + \frac{1}{2L}\Phi^2(t), \tag{2.9}$$

where $Q(t) = \partial \mathcal{L}_{\rm R}(t)/\partial\dot{\Phi}(t)$ is the *conjugate* charge corresponding to $\Phi(t)$. To quantize this Hamiltonian, the variables $Q(t)$ and $\Phi(t)$ are replaced by quantum operators $\hat{\Phi}$ and $\hat{Q}$ which obey the *canonical commutation relation* $\left[\hat{\Phi}, \hat{Q}\right] = i\hbar$. The quantum Hamiltonian reads

$$\hat{H}_{\rm R}(t) = \frac{1}{2C_\Sigma}\hat{Q}^2 + \frac{1}{2}C_\Sigma\omega_0^2\hat{\Phi}^2 - \frac{C_g v(t)}{C_\Sigma}\hat{Q}, \tag{2.10}$$

with the resonant (angular) frequency $\omega_0 = 1/\sqrt{LC_\Sigma}$. We can easily rewrite the quantum Hamiltonian in terms of harmonic oscillator creation and annihilation operators [10],

$$\hat{H}_{\rm R}(t) = \hbar\omega_0\left(\hat{a}^\dagger\hat{a} + \frac{1}{2}\right) - i\hbar\chi(t)\left(\hat{a}^\dagger - \hat{a}\right), \tag{2.11}$$

where

$$\chi(t) \equiv \frac{v(t)C_g}{\hbar C_\Sigma}\sqrt{\frac{C_\Sigma\hbar\omega_0}{2}} = v(t)C_g\sqrt{\frac{\omega_0}{2\hbar C_\Sigma}}. \tag{2.12}$$

The time evolution of density matrix of the resonator $\hat{\rho}_{\rm R}$ is governed by the matrix form Schrödinger equation (also known as the *Liouville-von Neumann equation*)

$$i\hbar\dot{\hat{\rho}}_{\rm R}(t) = \left[\hat{H}_{\rm R}(t), \hat{\rho}_{\rm R}(t)\right]. \tag{2.13}$$

If we rewrite the Hamiltonian Eq. (2.11) as $\hat{H}_{\rm R}(t) = \hat{H}_0 + \hat{H}_{\rm Int}(t)$, with

$$\hat{H}_0 = \hbar\omega_0\left(\hat{a}^\dagger\hat{a} + \frac{1}{2}\right) \text{ and } \hat{H}_{\rm Int}(t) = -i\hbar\chi(t)\left(\hat{a}^\dagger - \hat{a}\right), \tag{2.14}$$

we may bring the system into the *interaction picture*, and write the Liouville-von Neumann equation in this picture as

$$i\hbar\dot{\hat{\tilde{\rho}}}_{\rm R}(t) = \left[\hat{\tilde{H}}_{\rm Int}(t), \hat{\tilde{\rho}}_{\rm R}(t)\right], \tag{2.15}$$

where $\hat{\tilde{\rho}}_{\rm R}(t) = \exp\left(i\hat{H}_0 t/\hbar\right)\hat{\rho}_{\rm R}(t)\exp\left(-i\hat{H}_0 t/\hbar\right)$, and

$$\hat{\tilde{H}}_{\rm Int}(t) = \exp\left(\frac{i\hat{H}_0 t}{\hbar}\right)\hat{H}_{\rm Int}(t)\exp\left(-\frac{i\hat{H}_0 t}{\hbar}\right) = -i\hbar\chi(t)\left(\hat{a}^\dagger e^{i\omega_0 t} - \hat{a}e^{-i\omega_0 t}\right). \tag{2.16}$$

By substituting the equivalent integral form of Eq. (2.15) [9, 13]

$$\hat{\tilde{\rho}}_{\rm R}(t) = \hat{\tilde{\rho}}_{\rm R}(0) - \frac{i}{\hbar}\int_0^t dt'\left[\hat{\tilde{H}}_{\rm Int}(t'), \hat{\tilde{\rho}}_{\rm Int}(t')\right] \tag{2.17}$$

into Eq. (2.15), the interaction picture Liouville-von Neumann equation reads

$$i\hbar\dot{\hat{\tilde{\rho}}}_{\rm R}(t) = \left[\hat{\tilde{H}}_{\rm Int}(t), \hat{\tilde{\rho}}_{\rm R}(0)\right] - \frac{i}{\hbar}\int_0^t dt' \left[\hat{\tilde{H}}_{\rm Int}(t), \left[\hat{\tilde{H}}_{\rm Int}(t'), \hat{\tilde{\rho}}_{\rm R}(t')\right]\right]. \tag{2.18}$$

2.1.1 LC resonator driven by noise

Considering that $v(t)$ is a noise voltage with zero mean, we can rewrite Eq. (2.18) as

$$\begin{aligned}\dot{\hat{\tilde{\rho}}}_{\rm R}(t) \;\approx\; -\sum_{m,n=1}^{2}\int_0^t dt' \Big\{ &\left[\hat{s}_n(t')\hat{\tilde{\rho}}_{\rm R}(t')\hat{s}_m(t) - \hat{s}_m(t)\hat{s}_n(t')\hat{\tilde{\rho}}_{\rm R}(t')\right]\langle\chi(t)\chi(t')\rangle \\ &+ \left[\hat{s}_m(t)\hat{\tilde{\rho}}_{\rm R}(t')\hat{s}_n(t') - \hat{\tilde{\rho}}_{\rm R}(t')\hat{s}_n(t')\hat{s}_m(t)\right]\langle\chi(t')\chi(t)\rangle\Big\},\end{aligned} \tag{2.19}$$

with $\hat{s}_1(t) \equiv \hat{a}^\dagger e^{i\omega_0 t}$, $\hat{s}_2(t) \equiv -\hat{a}e^{-i\omega_0 t}$, $\langle\chi(t)\chi(t')\rangle = \frac{C_g^2\omega_0}{2\hbar C_\Sigma}\langle v(t)v(t')\rangle$, and $\langle\chi(t')\chi(t)\rangle = \frac{C_g^2\omega_0}{2\hbar C_\Sigma}\langle v(t')v(t)\rangle$.

Now we assume that the autocorrelation function is only dependent on the time difference $\tau = t - t'$, $\langle v(t)v(t')\rangle = \langle v(\tau)v(0)\rangle$. We also make a *Markov approximation* [9, 13] to replace $\hat{\tilde{\rho}}_{\rm R}(t')$ by $\hat{\tilde{\rho}}_{\rm R}(t)$, based on the assumption that the correlation time of the noise voltage is much shorter than the relaxation time (to be defined later) of the resonator[2]. We can then write Eq. (2.19) explicitly as

$$\begin{aligned}\dot{\hat{\tilde{\rho}}}_{\rm R}(t) \;\approx\; \frac{C_g^2\omega_0}{4\hbar C_\Sigma}\Big\{ &S_v(-\omega_0)\left[2\hat{a}^\dagger\hat{\tilde{\rho}}_{\rm R}(t)\hat{a} - \hat{a}\hat{a}^\dagger\hat{\tilde{\rho}}_{\rm R}(t) - \hat{\tilde{\rho}}_{\rm R}(t)\hat{a}\hat{a}^\dagger\right] \\ &+ S_v(\omega_0)\left[2\hat{a}\hat{\tilde{\rho}}_{\rm R}(t)\hat{a}^\dagger - \hat{\tilde{\rho}}_{\rm R}(t)\hat{a}^\dagger\hat{a} - \hat{a}^\dagger\hat{a}\hat{\tilde{\rho}}_{\rm R}(t)\right]\Big\},\end{aligned} \tag{2.20}$$

where the noise spectral density $S_v(\pm\omega_0) \equiv \int_{-\infty}^{\infty} d\tau e^{\pm i\omega_0\tau}\langle v(\tau)v(0)\rangle$. Here the fast oscillating terms with $\exp(\pm 2i\omega_0 t)$ are neglected. On the right-hand side of the equation above, the first and second lines describe excitation and relaxation of the resonator, respectively.

For a classical noise, the excitation and relaxation rates in Eq. (2.20) are the same, since $S_v(\omega_0) = S_v(-\omega_0)$; whereas for a quantum noise, they are not equal. Without loss of generality, we consider the quantum noise voltage across a linear dissipative element at thermal equilibrium. In the Caldeira-Leggett representation (see [11]), the quantum noise spectral densities at $\pm\omega_0$ are

$$\begin{aligned}S_v(\omega_0) &= \hbar\omega_0\Re[Z(\omega_0)]\left[\coth\left(\frac{\hbar\omega_0}{2k_BT}+1\right)\right] = 2\hbar\omega_0 R_0\frac{1}{1-\exp[-\hbar\omega_0/(k_BT)]}, \\ S_v(-\omega_0) &= -\hbar\omega_0\Re[Z(-\omega_0)]\left[\coth\left(\frac{-\hbar\omega_0}{2k_BT}+1\right)\right] = 2\hbar\omega_0 R_0\frac{1}{\exp[\hbar\omega_0/(k_BT)]-1},\end{aligned}$$

[2]For a thermal noise, which is approximately white, the Markov approximation is quite reasonable since the autocorrelation function is approximately a Dirac delta function, $\langle v(t)v(t')\rangle \propto \delta(t-t')$. In the Caldeira-Leggett representation, the Markov approximation also holds for harmonic reservoir (see Chapter 1).

where k_B is the Boltzmann constant, $Z(\omega)$ is the impedance function of the dissipative element, $\Re[Z(\omega_0)] = \Re[Z(-\omega_0)] \equiv R_0$, $\{\exp[\hbar\omega_0/(k_BT)] - 1\}^{-1} = \bar{n}$ is the mean number of quanta in the harmonic mode ω_0, and $\{1 - \exp[-\hbar\omega_0/(k_BT)]\}^{-1} = \bar{n} + 1$. Eq. (2.20) can now be rewritten as

$$\begin{aligned}\dot{\hat{\tilde{\rho}}}_{\rm R}(t) &= \frac{\gamma}{2}\bar{n}\left[2\hat{a}^\dagger\hat{\tilde{\rho}}_{\rm R}(t)\hat{a} - \hat{a}\hat{a}^\dagger\hat{\tilde{\rho}}_{\rm R}(t) - \hat{\tilde{\rho}}_{\rm R}(t)\hat{a}\hat{a}^\dagger\right] \\ &\quad + \frac{\gamma}{2}(\bar{n}+1)\left[2\hat{a}\hat{\tilde{\rho}}_{\rm R}(t)\hat{a}^\dagger - \hat{\tilde{\rho}}_{\rm R}(t)\hat{a}^\dagger\hat{a} - \hat{a}^\dagger\hat{a}\hat{\tilde{\rho}}_{\rm R}(t)\right], \end{aligned} \tag{2.21}$$

with the relaxation rate $\gamma = R_0\omega_0^2C_g^2/C_\Sigma$. The relaxation time is defined as γ^{-1}.

Transforming Eq. (2.21) back to the *Schrödinger picture*, we obtain the master equation for a resonator driven by (quantum) noise,

$$\begin{aligned}\dot{\hat{\rho}}_{\rm R}(t) &= -i\omega_0\left[\hat{a}^\dagger\hat{a}, \hat{\rho}_{\rm R}(t)\right] + \frac{\gamma}{2}(\bar{n}+1)\left[2\hat{a}\hat{\rho}_{\rm R}(t)\hat{a}^\dagger - \hat{a}^\dagger\hat{a}\hat{\rho}_{\rm R}(t) - \hat{\rho}_{\rm R}(t)\hat{a}^\dagger\hat{a}\right] \\ &\quad + \frac{\gamma}{2}\bar{n}\left[2\hat{a}^\dagger\hat{\rho}_{\rm R}(t)\hat{a} - \hat{a}\hat{a}^\dagger\hat{\rho}_{\rm R}(t) - \hat{\rho}_{\rm R}(t)\hat{a}\hat{a}^\dagger\right]. \end{aligned} \tag{2.22}$$

2.1.2 Damped resonator with sinusoidal drive

If we take an extra monochromatic *ac* driving voltage, $v_0\sin(\omega_d t)$, of constant amplitude v_0 and oscillating frequency ω_d into account, we can write the master equation for the driven resonator as [14]

$$\begin{aligned}\dot{\hat{\rho}}_{\rm R}(t) &\approx -i\omega_0\left[\hat{a}^\dagger\hat{a}, \hat{\rho}_{\rm R}(t)\right] - \chi_0\sin(\omega_d t)\left[\hat{a}^\dagger - a, \hat{\rho}_{\rm R}(t)\right] \\ &\quad + \frac{\gamma}{2}(\bar{n}+1)\left[2\hat{a}\hat{\rho}_{\rm R}(t)\hat{a}^\dagger - \hat{a}^\dagger\hat{a}\hat{\rho}_{\rm R}(t) - \hat{\rho}_{\rm R}(t)\hat{a}^\dagger\hat{a}\right] \\ &\quad + \frac{\gamma}{2}\bar{n}\left[2\hat{a}^\dagger\hat{\rho}_{\rm R}(t)\hat{a} - \hat{a}\hat{a}^\dagger\hat{\rho}_{\rm R}(t) - \hat{\rho}_{\rm R}(t)\hat{a}\hat{a}^\dagger\right], \end{aligned} \tag{2.23}$$

where $\chi_0 = v_0C_g\sqrt{\omega_0/(2\hbar C_\Sigma)}$, and $|\chi_0| \ll \omega_0$ is assumed.

From Eq. (2.23), we can obtain the equations of motion for $\langle\hat{a}^\dagger\rangle = \mathrm{tr}[\hat{a}^\dagger\rho_{\rm R}(t)]$ and $\langle\hat{a}\rangle = \mathrm{tr}[\hat{a}\rho_{\rm R}(t)]$:

$$\frac{d}{dt}\langle\hat{a}^\dagger\rangle = \left(i\omega_0 - \frac{\gamma}{2}\right)\langle\hat{a}^\dagger\rangle - \chi_0\sin(\omega_d t), \tag{2.24}$$

$$\frac{d}{dt}\langle\hat{a}\rangle = -\left(i\omega_0 + \frac{\gamma}{2}\right)\langle\hat{a}\rangle - \chi_0\sin(\omega_d t). \tag{2.25}$$

By solving these two equations, a very important physical quantity, the mean displacement of the driven oscillation

$$\langle\hat{\Phi}\rangle = \sqrt{\frac{\hbar}{2C_\Sigma\omega_0}}\left(\langle\hat{a}^\dagger\rangle + \langle\hat{a}\rangle\right), \tag{2.26}$$

can then be calculated for arbitrary time t. It turns out that $\langle\hat{\Phi}\rangle$ oscillates at the driving frequency ω_d with a phase difference

$$\beta = \arctan\left[\frac{\gamma\left(\gamma^2 + 4\omega_0^2 + 4\omega_d^2\right)}{2\omega_d\left(\gamma^2 - 4\omega_0^2 + 4\omega_d^2\right)}\right] \tag{2.27}$$

relative to the driving voltage (the explicit expression of $\langle\hat{\Phi}\rangle$ can be found in Appendix A).

From the average displacement $\langle\hat{\Phi}\rangle$, we can calculate one experimentally measurable quantity, the average (over one period of oscillation[3]) amount of energy absorbed by the resonator per unit time (the power absorbed by the resonator) [12] (in terms of the number of quanta $\hbar\omega_0$)

$$\begin{aligned} n(\omega_d) &= \frac{\gamma C_\Sigma \omega_d}{\pi\hbar\omega_0}\int_0^{2\pi/\omega_d} dt\left(d\langle\hat{\Phi}\rangle/dt\right)^2 \\ &= \frac{8\gamma\chi_0^2\omega_d^2\left(\gamma^2+4\omega_d^2\right)}{\omega_0^2\left[\gamma^4+16\left(\omega_0^2-\omega_d^2\right)^2+8\gamma^2\left(\omega_0^2+\omega_d^2\right)\right]}. \end{aligned} \tag{2.28}$$

For low dissipation $\gamma \ll \omega_0, \omega_d$, and small detuning between the driving frequency and the resonant frequency $|\omega_d - \omega_0| \ll \omega_0, \omega_d$, the relative phase is approximately $\beta = \arctan\left[\gamma/(2\omega_d - 2\omega_0)\right]$, and the mean number of quanta absorbed per unit time is reduced to

$$n(\omega_d) \approx \frac{2\gamma\chi_0^2}{\gamma^2 + 4(\omega_d-\omega_0)^2}, \tag{2.29}$$

which represents a Lorentzian line shape centered at ω_0 and with full width at half maximum (FWHM) of γ. In Fig. 2.2, $n(\omega_d)$ and β are plotted as functions of the detuning $\omega_d - \omega_0$.

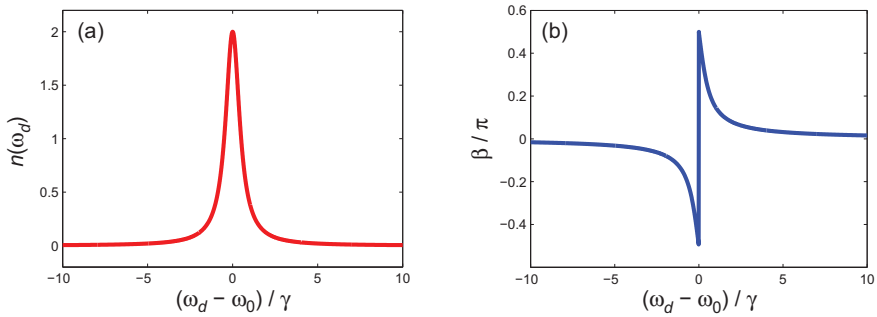

Figure 2.2. (a) The mean number of quanta n absorbed per γ^{-1} as a function of detuning. (b) The relative phase β of oscillation as a function of detuning. $\chi_0 = \gamma$ is taken.

The *external* quality factor Q_{ext} corresponding to the dissipation γ caused by the external voltage fluctuations can be defined as

$$Q_{ext} \equiv \omega_0/\gamma = C_\Sigma/(R_0\omega_0 C_g^2). \tag{2.30}$$

[3]In real experiments, averaging over many oscillation periods may be needed, but mathematically there is no difference between averaging over several periods and over just one period.

Since the characteristic impedance of the *LC* resonator is $Z_0 \approx \sqrt{L/C_\Sigma}$, the total capacitance C_Σ can be written as $C_\Sigma = 1/(\omega_0 Z_0)$. Substituting it into Eq. (2.30), we obtain

$$Q_{ext} \approx 1 \,/\, \left(R_0 Z_0 C_g^2 \omega_0^2\right) . \tag{2.31}$$

2.2 Experimental point of view

In the previous section we have discussed a lumped-element model of an electromagnetic resonator. In experiments, it is quite common to use a coplanar waveguide (CPW) [15] design in which the capacitance and inductance are evenly distributed along a metallic stripline, separated by a pair of ground planes (see the inset at the top-left corner of Fig. 2.3), with a length D comparable to the *guide* wavelength λ at resonant frequency ω_0. As an example, Fig. 2.3 shows a schematic design of a quarter-wavelength ($\lambda/4$) [16] CPW resonator.

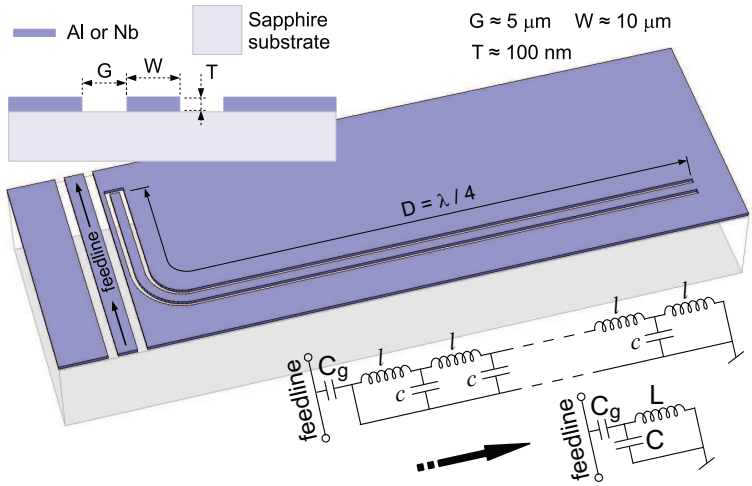

Figure 2.3. Schematic of a superconducting $\lambda/4$ CPW resonator capacitively coupled to a feedline (another CPW transmission line). It is equivalent to the lumped-element *LC* resonator. Insets: (top left) the cross section of a CPW on top of a dielectric substrate; (bottom right) circuit diagram of the $\lambda/4$ CPW resonator.

The way to derive the quantum Hamiltonian of a CPW resonator can be found in Appendix A of Publication **I**, and it is fully compatible with the method developed in the previous section. For the $\lambda/4$ resonator, the *fundamental mode*[4] effective

[4]Unlike in the lumped-element model, here Φ is not only dependent on time t, but also a function of location x on the CPW. Due to the boundary conditions $\partial\Phi(x,t)/\partial x = 0$ at open end (where C_g located, $x = 0$) and $\Phi(x,t) = 0$ at short end (ground end, $x = D$), $\Phi(x,t)$ can

capacitance and inductance are

$$C = Dc/2 \text{ and } L = 8Dl/\pi^2, \tag{2.32}$$

respectively. The resonant frequency is then

$$\omega_0 \approx 1/\sqrt{LC} = 2\pi \Big/ \left(4D\sqrt{lc}\right), \tag{2.33}$$

if $C_g \ll C$. Here l and c are the *geometric* inductance and capacitance per unit length, respectively (see the bottom right inset of Fig. 2.3).

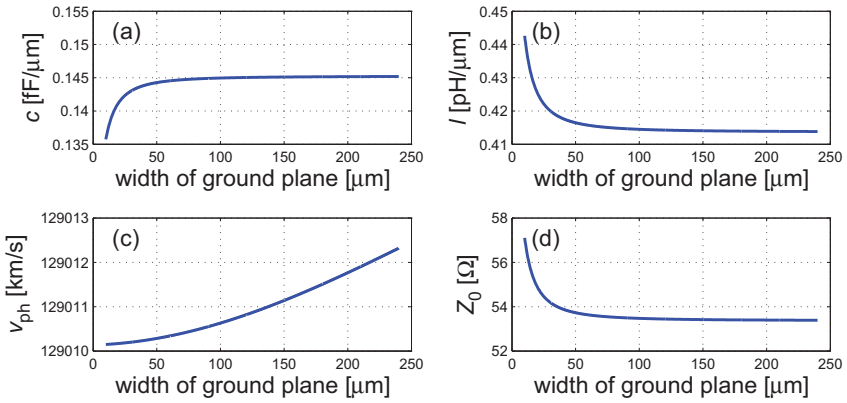

Figure 2.4. (a) Geometric capacitance per unit length c, (b) geometric inductance per unit length l, (c) phase velocity $v_{\rm ph}$, and (d) characteristic impedance Z_0 as functions of the ground plane width. A value of the relative permittivity $\varepsilon_r = 9.8$ for the sapphire substrate is used.

One advantage of using the CPW design is that the geometric inductance l and capacitance c per unit length can be calculated accurately by using the finite-element method [17]. Fig. 2.4 (a) and (b) show the numerical results of c and l, respectively, for the CPW samples we have been using: about 100 nm thick single layer aluminum or niobium film with stripline width $W \approx 10$ μm and gap width $G \approx 5$ μm deposited on top of 330 μm thick sapphire substrate (see also Fig. 2.3).

In real samples the stripline is normally twisted (see Fig. 2.5), due to the fact that the length D is much longer than the size of the chip. The width of ground plane between two parallel ports of the stripline may not be considered as semi-infinite, therefore here c and l are calculated with varying ground plane width. Besides, the phase velocity $v_{\rm ph}$ and the characteristic impedance Z_0,

$$v_{\rm ph} = 1/\sqrt{lc} \text{ and } Z_0 = \sqrt{l/c}, \tag{2.34}$$

be decomposed as $\Phi(t)\cos(k_n x)$, with $k_n = n\pi/(2D)$. $n = 1, 2, \ldots$ is the mode number. For more details see Appendix A of Publication **I**.

are also shown in Fig. 2.4 (c) and (d), respectively. Data in Fig. 2.4 clearly indicates that for a width of the ground plane larger than about 100 μm, l and c are almost width independent.

Another advantage of the CPW design is its uniplanar structure, which really simplifies the fabrication processes. A CPW resonator can be fabricated in two or three steps, depending on the superconducting material been used. Aluminum and niobium are two frequently used superconductors for making both resonators and Josephson junctions. Aluminum resonators can be fabricated by a physical vapor deposition process [18] followed by a conventional lithography process [19]. Making niobium resonators is a bit more complicated, due to the difficulty of getting high quality niobium thin films by physical vapor deposition. A typical procedure of making niobium resonators uses the reaction ion etching (RIE) of the gap areas patterned on the DC sputtered [18] niobium film by lithography process.

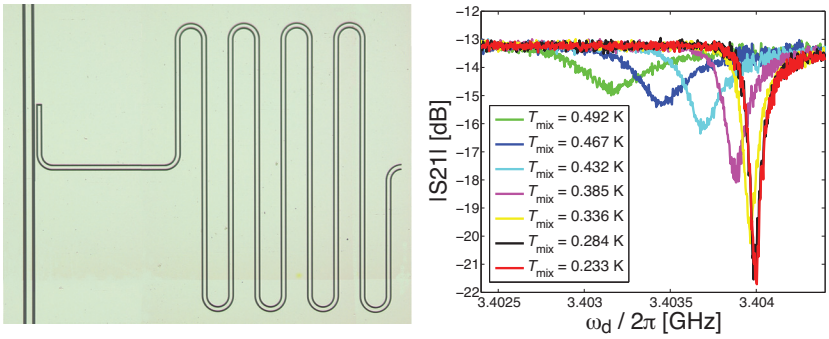

Figure 2.5. Left: Optical microscopic picture of a $\lambda/4$ aluminum resonator on top of a sapphire substrate. The total length of the resonator D is approximately 8.6 mm, and the size of the sapphire chip is 5×5 mm. Right: The magnitude of microwave transmission coefficient S21 through the feedline capacitively coupled to this $\lambda/4$ resonator as a function of microwave frequency ω_d, measured at different mixing chamber temperature $T_{\rm mix}$.

On the left-hand side of Fig. 2.5, a 8.6 mm long $\lambda/4$ aluminum resonator and a CPW feedline (see the illustrations of Fig. 2.3) on top of a sapphire substrate are shown. The CPWs were patterned by electron beam (ebeam) lithography with tri-layer ebeam resists: a layer of conducting resist, ESPACER300 [20], on top of standard PMMA/Copolymer bi-layer [21]. The 100 nm thick aluminum film was deposited in a ultra-high vacuum (UHV) electron gun evaporator. This sample was measured at low temperature by mounting it at the mixing chamber of a dilution refrigerator (a sketch of a similar measurement setup can be found in Fig. 6.2 of Chapter 6).

The power absorbed by the resonator is measured in terms of the energy loss of

a microwave at frequency ω_d sent through the feedline. This is characterized by the magnitude of a scattering parameter S21 (normally in logarithmic scale) in microwave engineering [16], as shown on the right-hand side of Fig. 2.5. The magnitude of S21 has the same line shape (but flipped upside down) as that of the resonator's power absorption [see Fig. 2.2 (a)]. Besides, there is a temperature ($T_{\rm mix}$) dependence of the resonant frequency due to the *kinetic* inductance per unit length $l_{\rm k}$ of the aluminum stripline [22], which should be added to the geometric inductance per unit length l shown in Fig. 2.4 (b). When the mixing chamber temperature $T_{\rm mix}$ is well below the critical temperature T_c of the aluminum film, $T_{\rm mix} \ll T_c$, by taking $l \approx 0.415$ pH/μm, $c \approx 0.145$ fF/μm, and $\omega_0 \approx 2\pi \times 3.404$ GHz, the kinetic inductance per unit length for this sample is estimated as $l_{\rm k} \approx 0.088$ pH/μm from Eq. (2.33), which is much smaller than the geometric inductance per unit length l.

The measured *loading* quality factor at low $T_{\rm mix}$ for this sample is $Q_L \approx 7 \times 10^4$. The coupling capacitance between the resonator and the feedline in this sample is $C_g \approx 2$ fF (estimated by using the finite-element method). By using Eq. (2.31) we obtain the external quality factor $Q_{ext} \approx 2 \times 10^5$, and by using [22]

$$\frac{1}{Q_L} = \frac{1}{Q_{ext}} + \frac{1}{Q_{int}}, \tag{2.35}$$

we can roughly estimate the *internal* quality factor Q_{int} due to the internal dissipation of the resonator.

3. Artificial Atoms Based on Josephson Junctions

In this chapter, I will give a brief review of superconducting artificial atoms (*qudits*[1]) and devices based on Josephson junctions, but not an introduction of the Josephson junction (or the Josephson effect) itself. One can find a very nice presentation of the Josephson effect in classic books such as [23] by Likharev and [24] by Tinkham.

Let us forget about the Josephson junction for a while and step back to the lumped-element model of a *LC* resonator we studied in Sec. 2.1. In order to construct an artificial atom from it, we need to introduce anharmonicity into the circuit shown in Fig. 2.1. The straightforward way is to engineer the potential energy Eq. (2.5) by replacing the linear inductor with something nonlinear (we may call it a nonlinear inductor).

The *differential* inductance L_d of an inductor can be defined as [25]

$$L_d \equiv \partial\Phi_L(t)/\partial i_L(t) = \left[\partial i_L(t)/\partial\Phi_L(t)\right]^{-1}, \tag{3.1}$$

where the branch flux $\Phi_L(t)$ was defined in Eq. (2.3). Obviously, for a linear inductor of which the branch flux is linearly dependent on the current, $\Phi_L(t) = i_L(t)L$ (see Eq. (2.2) in Sec. 2.1), the differential inductance $L_d = L$.

Now we assume that we have such a nonlinear inductor that its current-flux relation consists of the linear one shown above and a quadratic perturbation[2],

$$i_L(t) = \frac{\varphi_0}{L}\left[\phi_L(t) + \varepsilon\phi_L^2(t)\right], \tag{3.2}$$

with a real factor $\varepsilon \ll 1$. Here, in order to make sure that the dimension is conserved, I have defined a dimensionless branch flux $\phi_L(t) \equiv \Phi_L(t)/\varphi_0$, where φ_0 can

[1] All superconducting artificial atoms are multilevel quantum systems. "qudit"is a general name for a d-level quantum system. Depending on applications, a qudit can be truncated to either a two-level system ($d = 2$), namely a *qubit*, or a three-level system ($d = 3$), namely a *qutrit*.

[2] A general nonlinear current-flux relation can be $i_L(t) = (\varphi_0/L)\sum_{k=1}^{\infty}\varepsilon_k\phi_L^k(t)$. Here let us only consider a simple case.

be considered as the *elementary* flux (just like that a charge Q can be defined, in terms of a dimensionless number q and the *elementary* charge e, as $Q = qe$).

By using the definition in Eq. (3.1), the differential inductance for the nonlinear inductor is obtained as

$$L_d = L/[1 + 2\varepsilon\phi_L(t)]. \tag{3.3}$$

The potential energy then has a cubic form

$$E_L = \varphi_0 \int_{-\infty}^{t} \dot{\phi}_L(\tau) i_L(\tau) d\tau = \frac{\varphi_0^2}{L}\left[\frac{1}{2}\phi_L^2(t) + \frac{\varepsilon}{3}\phi_L^3(t)\right]. \tag{3.4}$$

Replacing the linear inductance L in Fig. 2.1 with the nonlinear inductance L_d given by Eq. (3.3) does not change the capacitive energies E_C, E_g given by Eq. (2.4) and the voltage constrains in Eq. (2.6), therefore the new Hamiltonian can be easily obtained by substituting Eq. (3.4) for the last term in Eq. (2.9),

$$H_{\mathrm{R}}(t) = \frac{e^2}{2C_\Sigma}[q - q_g(t)]^2 + \frac{\varphi_0^2}{L}\left(\frac{1}{2}\phi^2 + \frac{\varepsilon}{3}\phi^3\right), \tag{3.5}$$

where $q_g(t) = C_g v(t)/e$, $q = Q/e$, and $\phi \equiv \phi_L = \Phi/\varphi_0$.

On the left-hand side of Fig. 3.1 shown below, the dimensionless potential energy $E_L/(\varphi_0^2/L)$ is plotted for different values of ε. For non-zero ε, this potential looks very similar to that of a Josephson phase qubit as shown on the right-hand side of Fig. 3.1. However, one should note that the "ϕ" in the Josephson phase qubit potential (right-hand side of Fig. 3.1) represents the *gauge-invariant* phase difference [24] across the Josephson junction. Is it the same as the dimensionless branch flux "ϕ"?

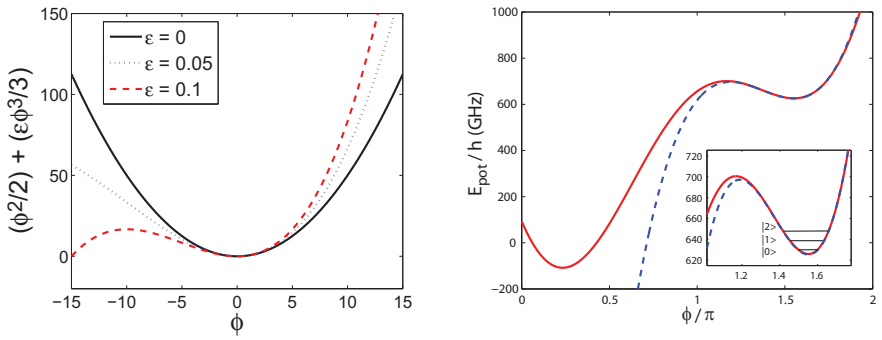

Figure 3.1. Left: Dimensionless potential energy $E_L/(\varphi_0^2/L)$ as a function of the dimensionless branch flux ϕ, for different values of ε. Right: The potential energy of a typical Josephson phase qubit (the red solid curve) and its cubic approximation (the blue dashed curve), taken from Fig. 2 of Publication **VI**.

Let us consider a superconductor-insulator-superconductor (SIS) Josephson junction (see *e.g.* Fig. 6.1 in [24]) which is widely used for superconducting qubits.

When a voltage difference $v_J(t)$ is maintained across the junction, the Josephson voltage-phase relation [24] holds,

$$\frac{2e}{\hbar}v_J(t) = \frac{d\Delta\varphi(t)}{dt} = \frac{d\phi(t)}{dt}, \tag{3.6}$$

where $\Delta\varphi$ is the Ginzburg-Landau "wavefunciton" phase difference across the junction, ϕ is the gauge-invariant phase difference, and $\Delta\varphi = \phi \pmod{2\pi}$. The branch flux for this junction is then

$$\Phi_J(t) = \int_{-\infty}^{t} v_J(\tau)d\tau = \frac{\hbar}{2e}\phi(t). \tag{3.7}$$

If the *elementary* flux [see the discussion below Eq. (3.2)] is defined as $\varphi_0 = \hbar/(2e) = \Phi_0/(2\pi)$, which is known as the reduced magnetic flux quantum, the gauge-invariant phase difference is then the same as the dimensionless branch flux. By further considering the Josephson current-phase relation $i_J = i_0 \sin\phi$, with supercurrent i_J and critical current i_0, respectively, we can also obtain the differential Josephson inductance

$$L_J = [\partial i_J/\partial\Phi_J]^{-1} = L_{J0}/\cos\phi, \tag{3.8}$$

with $L_{J0} = \varphi_0/i_0$. The stored energy of this Josephson junction is then

$$E_J = \int_{-\infty}^{t} v_J(\tau)i_J(\tau)d\tau = -E_{\mathrm{J0}}\cos\phi, \tag{3.9}$$

where $E_{\mathrm{J0}} = i_0\varphi_0$ is the so-called Josephson energy.

3.1 The Cooper-pair box

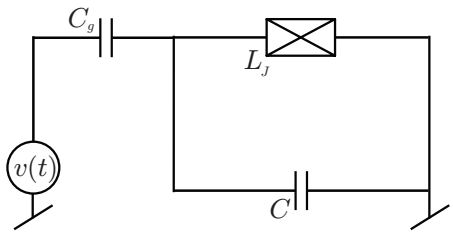

Figure 3.2. A voltage biased CPB qubit, obtained by replacing the linear inductor L in Fig. 2.1 with the Josephson junction L_J.

By substituting Eq. (3.9) into Eq. (3.5), we obtain the Hamiltonian

$$H(t) = E_{\mathrm{C}}\left[q - q_g(t)\right]^2 - E_{\mathrm{J0}}\cos\phi \tag{3.10}$$

for a circuit which is called a Cooper-pair box (CPB), as shown in Fig. 3.2. Here we redefine the dimensionless charges $q \equiv Q/(2e)$, $q_g(t) \equiv C_g v(t)/(2e)$, and the charging energy $E_\mathrm{C} \equiv (2e)^2/(2C_\Sigma)$.

The quantum Hamiltonian of this CPB can be written, in the charge eigenbasis $|q\rangle$ [11], as

$$\begin{aligned} \hat{H} &= E_\mathrm{C}\left(\hat{q}-q_g\right)^2 - E_{\mathrm{J}0}\cos\hat{\phi} \\ &= \sum_{q=-\infty}^{+\infty}\left[E_\mathrm{C}\left(q-q_g\right)^2|q\rangle\langle q| - \frac{E_{J0}}{2}\left(|q+1\rangle\langle q| + |q-1\rangle\langle q|\right)\right]. \end{aligned} \tag{3.11}$$

In Fig. 3.3, four lowest eigenenergy levels of the quantum Hamiltonian for various q_g are plotted in (a) charge regime ($E_\mathrm{C} \gg E_{\mathrm{J}0}$) and (b) phase regime ($E_\mathrm{C} \ll E_{\mathrm{J}0}$).

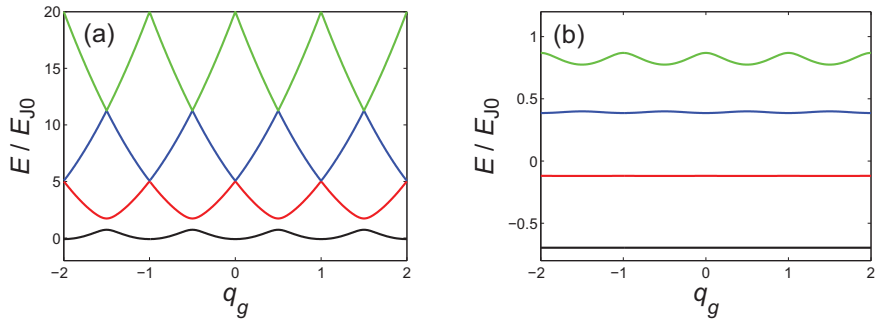

Figure 3.3. The eigenenergies of a CPB as a function of gate charge q_g for (a) $E_\mathrm{C} = 5E_{\mathrm{J}0}$ and (b) $E_\mathrm{C} = 0.2E_{\mathrm{J}0}$.

In the charge regime, the CPB is also known as a *charge* qubit. The first experimentally realized superconducting artificial atom [26] was a charge qubit. However, in recent years, the charge qubit design has been abandoned, because of its short decoherence time due to the strong q_g dependence of the eigenenergies, as shown in Fig. 3.3 (a). Truncating Eq. (3.11) to the two adjacent charge states $|q\rangle$ and $|q+1\rangle$, the quantum Hamiltonian can be written as

$$\hat{H} = E_\mathrm{C}\left[q_g - \left(q+\frac{1}{2}\right)\right]\hat{\sigma}_z - \frac{E_{\mathrm{J}0}}{2}\hat{\sigma}_x, \tag{3.12}$$

where the Pauli matrices $\hat{\sigma}_z \equiv |q\rangle\langle q| - |q+1\rangle\langle q+1|$, $\hat{\sigma}_x \equiv |q+1\rangle\langle q| + |q\rangle\langle q+1|$, and $q \le q_g \le q+1$. For q_g close to either q or $q+1$, the eigenstates of Eq. (3.12) are equivalent to the charge states, as shown in Fig. 3.4. A gate charge fluctuation δq_g can easily cause decoherence (in this case it is pure dephasing) [27, 28] of the qubit. To improve the decoherence time, a variant of the charge qubit called *quantronium* was developed in 2002 [29]. It works in the charge-phase regime ($E_\mathrm{C} \sim E_{\mathrm{J}0}$), in which the eigenenergies are smoother than those in the charge

regime. To minimize the decoherence induced by the gate charge fluctuations, the quantronium is always *dc* biased at half-integer gate charges (charge degeneracy points) where the two lowest eigenenergy levels are separated by the Josephson energy $E_{\mathrm{J}0}$ (see Fig. 3.4).

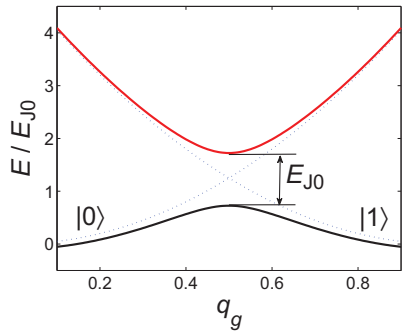

Figure 3.4. The eigenenergies (solid curves) of a charge qubit for $E_{\mathrm{C}} = 5E_{\mathrm{J}0}$ and $q = 0$. At $|q_g - 1/2| \gg 0$, the charge states $|0\rangle$ and $|1\rangle$ have energies (dotted curves) similar to the eigenenergies; at the charge degeneracy point, $q_g = 1/2$, the eigenenergy gap is equal to the Josephson energy $E_{\mathrm{J}0}$.

3.2 The transmon qubit

By further decreasing the charging energy to the phase regime, the CPB, instead of being named *phase* qubit, is called a *transmon* [30]. Comparing it with the quantronium, the transmon does not require a fixed *dc* voltage bias, since its eigenenergies (at least for the two lowest levels) are almost independent of q_g, as plotted in Fig. 3.3 (b). Technically, the charging energy is lowered by shunting the Josephson junction with an interdigitated capacitor. To gain extra tunability of the Josephson energy, the single Josephson junction is split into two and integrated in a small superconducting loop, as shown in Fig. 3.5.

The Hamiltonian of a transmon can be quantized in the same manner as the phase qutrit as discussed in Sec. II of Publication **VI**. We start with a classical Hamiltonian very similar to Eq. (3.10),

$$H = E_{\mathrm{C}}(q - q_g)^2 - E_{\mathrm{J}1}\cos\phi_1 - E_{\mathrm{J}2}\cos\phi_2, \tag{3.13}$$

with the Josephson energies $E_{\mathrm{J}1}$ and $E_{\mathrm{J}2}$ of the two Josephson junctions, respectively. ϕ_1 and ϕ_2 are the gauge-invariant phase differences across the two junctions, and they fulfill the fluxoid quantization condition

$$\phi_1 - \phi_2 = \Phi/\varphi_0 \ (\mathrm{mod}\ 2\pi), \tag{3.14}$$

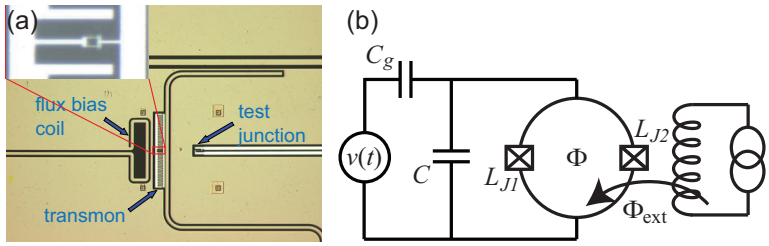

Figure 3.5. (a) Optical microscopic picture of a transmon qubit, fabricated by ebeam lithography and standard double-angle evaporation, embedded in a niobium $\lambda/4$ CPW resonator. (b) Equivalent circuit diagram of the transmon (ignoring the resonator here).

where Φ is the total magnetic flux through the loop, which is the sum of the external bias flux $\Phi_{\rm ext}$ and the screening flux $\Phi_{\rm s}$ [24]. Normally the loop inductance of a transmon is negligibly small, and therefore $\Phi \approx \Phi_{\rm ext}$. By defining

$$\phi \equiv (\phi_1 + \phi_2)/2, \quad E_{\rm J0} \equiv E_{\rm J1} + E_{\rm J2} \ \text{ and } \ d \equiv (E_{\rm J2} - E_{\rm J1})/E_{\rm J0} \ll 1, \tag{3.15}$$

the Hamiltonian Eq. (3.13) can be written as

$$H = E_{\rm C}(q - q_g)^2 - E_{\rm J0}\cos(\varphi_{\rm ext})\cos\phi - dE_{\rm J0}\sin(\varphi_{\rm ext})\sin\phi, \tag{3.16}$$

where $\varphi_{\rm ext} = \Phi_{\rm ext}/(2\varphi_0) \pmod{\pi}$. In order to minimize the effect of charge fluctuations, the external magnetic flux should be biased at $E_{\rm J0}|\cos(\varphi_{\rm ext})| \gg E_{\rm C}$. In this case local minima of the cosine potential $\cos\phi$ can be well approximated by a quartic function, and the Hamiltonian above is approximately

$$\begin{aligned} H \ &\approx \ E_{\rm C}q^2 + E_{\rm J0}|\cos(\varphi_{\rm ext})|\frac{\phi^2}{2} - E_{\rm J0}|\cos(\varphi_{\rm ext})|\frac{\phi^4}{24} \\ &\quad -dE_{\rm J0}\sin(\varphi_{\rm ext})\left(\phi - \frac{\phi^3}{6}\right) - 2E_{\rm C}qq_g. \end{aligned} \tag{3.17}$$

The quadratic term dominates the potential energy, thus Eq. (3.17) describes a perturbed harmonic oscillator similar to the example discussed at the beginning of this chapter.

Quantizing and rewriting the dimensionless operators $\hat{\phi}$ and $\hat{q}$ in terms of harmonic oscillator creation and annihilation operators

$$\hat{\phi} = \left[\frac{E_{\rm C}}{2E_{\rm J0}|\cos(\varphi_{\rm ext})|}\right]^{1/4}\left(\hat{b}^\dagger + \hat{b}\right) \ \text{ and } \ \hat{q} = i\left[\frac{E_{\rm J0}|\cos(\varphi_{\rm ext})|}{8E_{\rm C}}\right]^{1/4}\left(\hat{b}^\dagger - \hat{b}\right), \tag{3.18}$$

respectively, the quantum Hamiltonian reads

$$\begin{aligned} \hat{H} \ &\approx \ \hbar\omega_p\left(\hat{b}^\dagger\hat{b} + \frac{1}{2}\right) - \frac{E_{\rm C}}{48}\left(\hat{b}^\dagger + \hat{b}\right)^4 - d\sin(\varphi_{\rm ext})\left[\frac{E_{\rm C}E_{\rm J0}^3}{2|\cos(\varphi_{\rm ext})|}\right]^{1/4}\left(\hat{b}^\dagger + \hat{b}\right) \\ &\quad -iq_g\left[2E_{\rm C}^3E_{\rm J0}|\cos(\varphi_{\rm ext})|\right]^{1/4}\left(\hat{b}^\dagger - \hat{b}\right), \end{aligned} \tag{3.19}$$

with the plasma frequency

$$\omega_p = \sqrt{2E_{\rm C}E_{\rm J0}|\cos(\varphi_{\rm ext})|}\Big/\hbar. \tag{3.20}$$

Truncating it to the two lowest energy levels $\{|0\rangle, |1\rangle\}$, the Hamiltonian Eq. (3.19), in terms of Pauli matrices, has the form

$$\hat{H} = -\frac{\hbar\omega_{10}}{2}\hat{\sigma}_z - \frac{\hbar\Omega_x}{2}\hat{\sigma}_x - \frac{\hbar\Omega_y}{2}\hat{\sigma}_y, \tag{3.21}$$

where the $|0\rangle \leftrightarrow |1\rangle$ transition frequency $\omega_{10} = \omega_p - E_{\rm C}/(4\hbar)$, and

$$\hbar\Omega_x = 2d\sin(\varphi_{\rm ext})\left[\frac{E_{\rm C}E_{\rm J0}^3}{2|\cos(\varphi_{\rm ext})|}\right]^{1/4}, \quad \hbar\Omega_y = 2q_g\left[2E_{\rm C}^3E_{\rm J0}|\cos(\varphi_{\rm ext})|\right]^{1/4}. \tag{3.22}$$

In Fig. 3.6, the spectroscopy of the transmon used for motional averaging experiment (to be discussed in Chapter 6) is shown.

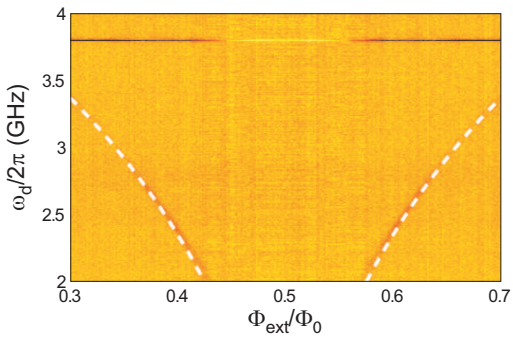

Figure 3.6. Transmon spectroscopy versus external flux bias $\Phi_{\rm ext}$. Dashed (white) curves: fittings of ω_{10} with $E_{\rm C}/\hbar = 2\pi \times 1.4$ GHz and $E_{\rm J0}/\hbar = 2\pi \times 8.4$ GHz.

3.3 The phase qutrit

A microscopic photo of a phase qutrit is shown in Fig. 3.7. In the *rf*-SQUID equivalent circuit of it, a single Josephson junction with a differential Josephson inductance L_J and a junction capacitance C has been inserted into a superconducting loop with inductance L.

Considering that the flux bias $\Phi_{\rm ext}$ consists of both the *dc* part $\Phi_{\rm dc}$ and the *rf* part $\Phi_{\rm rf}$, the classical Hamiltonian of the flux-biased *rf*-SQUID reads

$$H(t) = \frac{Q^2}{2C} + \frac{\Phi^2}{2L_J^*} + \frac{\Phi^3}{2\Phi_0 L^*} - \frac{\Phi\Phi_{\rm rf}(t)}{L}, \tag{3.23}$$

where the branch flux Φ of the Josephson junction and the charge Q accumulated on the capacitor are two canonically conjugate variables. L_J^* and L^* stand for the

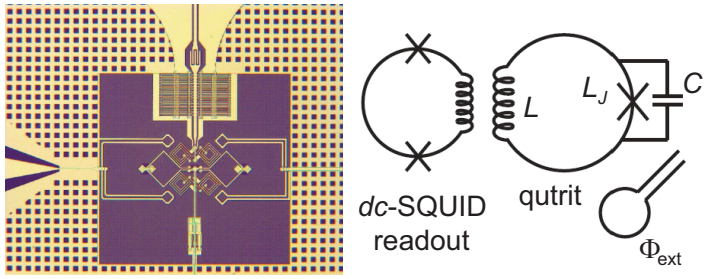

Figure 3.7. Left: Optical microscopic picture of a phase qubit sample from the National Institute of Standards and Technology (NIST), Boulder. Right: Schematics of the phase qubit and a nearby *dc*-SQUID for single-shot readout and on-chip flux bias circuit.

effective Josephson inductance and the effective loop inductance, respectively, and they are dependent on the *dc* flux bias (see Publication **VII**). The first three terms on the right-hand side of Eq. (3.23) are very similar to the terms on the right-hand side of Eq. (3.5).

A detailed derivation of quantum Hamiltonian for the phase qutrit is given in Publication **VII**. In the Autler-Townes splitting experiment (to be reviewed in Chapter 5) we only use the lowest three levels. The quantum Hamiltonian from Eq. (3.23) is

$$\hat{H}(t) = \begin{bmatrix} \hbar\omega_0/2 & 3\eta & 0 \\ 3\eta & 3\hbar\omega_0/2 & 6\sqrt{2}\eta \\ 0 & 6\sqrt{2}\eta & 5\hbar\omega_0/2 \end{bmatrix} - \frac{\Phi_{\rm rf}(t)}{L}\hat{\Phi}, \tag{3.24}$$

in the harmonic oscillator [formed by the first two terms on the right-hand side of Eq. (3.23)] eigenbasis $|n\rangle_0$, where $\omega_0 = \sqrt{1/(L_J^* C)}$ and $\eta = (\hbar/2C\omega_0)^{3/2}/(2\Phi_0 L^*)$. Since in the Autler-Townes experiment, η is only about 2% of $\hbar\omega_0$, the eigenstates $|n\rangle$ of the matrix on the right-hand side of Eq. (3.24) are quite close to the harmonic oscillator eigenstates $|n\rangle_0$. In the new basis $|n\rangle$, the quantum Hamiltonian can then be rewritten as

$$\hat{H}(t) \approx \hbar \begin{bmatrix} 0 & 0.69g(t) & 0.02g(t) \\ 0.69g(t) & \omega_{10} & g(t) \\ 0.02g(t) & g(t) & \omega_{10}+\omega_{21} \end{bmatrix}, \tag{3.25}$$

where $\omega_{10} \approx 0.976\omega_0$ and $\omega_{21} \approx 0.952\omega_0$ indicate the $|0\rangle \leftrightarrow |1\rangle$ and the $|1\rangle \leftrightarrow |2\rangle$ transition frequencies, respectively,

$$g(t) = -\frac{\Phi_{\rm rf}(t)}{L}\sqrt{\frac{1}{\hbar\omega_0 C}} \tag{3.26}$$

denotes the normalized *rf* driving field amplitude, and the factors in front of $g(t)$ are the dimensionless transition dipole moments.

In Fig. 3.8 below, a typical spectroscopy of a phase qutrit is presented. This spectroscopy shows the $|0\rangle \leftrightarrow |1\rangle$ and $|1\rangle \leftrightarrow |2\rangle$ transitions, as well as avoided crossings (red circled areas) due to the coupling between the qutrit and the two-level system (TLS) fluctuators inside the Josephson junction barrier (to be discussed in Chapter 4 and Chapter 6).

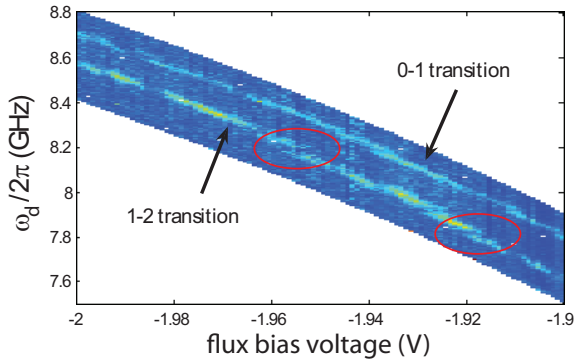

Figure 3.8. Phase qutrit spectroscopy versus external flux bias voltage. The avoided crossings (in the red circled areas) are caused by the transverse coupling to the TLSs.

3.4 Atom-resonator interaction — circuit QED

Superconducting circuits can be used to construct similar setups as traditional cavity QED in optical region. In Fig. 3.5(a), such a setup known as circuit QED [31, 32] was already presented. An artificial atom (a transmon qubit) is capacitively coupled to the center conductor of a CPW microwave resonator. If we consider that $v(t)$ in Fig. 3.5(b) is due to the microwave photons inside the resonator [33], $\hat{v} \approx i\sqrt{\hbar\omega_0/(Dc)}\left(\hat{a}^\dagger - \hat{a}\right)$ near the open end of the resonator (here ω_0 and Dc are the resonant frequency and the total capacitance of the resonator, respectively, see Sec. 2.2), and that the gate charge $\hat{q}_g = C_g\hat{v}/(2e)$, then from Eqs. (3.21) and (3.22) we can obtain the interaction Hamiltonian

$$\hat{H}_{\rm int} = -\frac{\hbar\hat{\Omega}_y}{2}\hat{\sigma}_y \approx \frac{C_g}{2e}\sqrt{\frac{\hbar\omega_0}{Dc}}\left[2E_{\rm C}^3 E_{\rm J0}|\cos(\varphi_{\rm ext})|\right]^{1/4}\left(\hat{\sigma}^+ - \hat{\sigma}^-\right)\left(\hat{a}^\dagger - \hat{a}\right), \qquad (3.27)$$

where $\hat{\sigma}^- \equiv |0\rangle\langle 1|$ and $\hat{\sigma}^+ \equiv |1\rangle\langle 0|$ are the qubit lowering and raising operators, respectively. By applying a rotating wave approximation [34], the interaction Hamiltonian takes the well known *Jaynes-Cummings* form

$$\hat{H}_{\rm int} \approx -\hbar\kappa\left(\hat{\sigma}^-\hat{a}^\dagger + \hat{\sigma}^+\hat{a}\right), \qquad (3.28)$$

with the coupling strength

$$\kappa = \frac{C_g}{2e}\sqrt{\frac{\omega_0}{\hbar D c}}\left[2E_{\rm C}^3 E_{\rm J0}|\cos(\varphi_{\rm ext})|\right]^{1/4}. \tag{3.29}$$

The total Hamiltonian, including the qubit, the resonator and the interaction reads

$$\hat{H} = -\frac{\hbar\omega_{10}}{2}\hat{\sigma}_z + \hbar\omega_0\left(\hat{a}^\dagger\hat{a} + \frac{1}{2}\right) - \hbar\kappa\left(\hat{\sigma}^-\hat{a}^\dagger + \hat{\sigma}^+\hat{a}\right). \tag{3.30}$$

For the transmon sample operating at $\omega_{10} \sim 2\pi \times 3$ GHz, and bare resonance of the resonator at $\omega_0 \approx 2\pi \times 3.8$ GHz (see Fig. 3.6), a strong coupling[3] $\kappa \sim 2\pi \times 100$ MHz ($C_g \sim 10$ fF) is achievable due to the transmon's large dimension. Recently, even the ultra-strong coupling regime $\kappa/\omega_0 > 0.1$ has been reached experimentally for a flux qubit inductively coupled either to a CPW resonator [35] or to a lumped *LC* resonator [36].

When the qubit and the resonator are near resonant, $\omega_{10} \approx \omega_0$, the interaction Hamiltonian in Eq. (3.28) couples the two product states $|0\rangle \otimes |n+1\rangle$ and $|1\rangle \otimes |n\rangle$ (here $|n\rangle$ and $|n+1\rangle$ indicate the eigenstates of the photon number operator $\hat{a}^\dagger\hat{a}$ of the resonator), and produces two *dressed states* [37] separated by an energy difference $\hbar\kappa\sqrt{n+1}$. This $\sqrt{n+1}$ dependence of the atom-photon coupling strength was observed in circuit QED in 2008 [38].

In the so called dispersive coupling regime [31], $|\omega_{10} - \omega_0| \gg \kappa$, we can perform a Schrieffer-Wolff transformation $\hat{U}^\dagger\hat{H}\hat{U}$ with operator

$$\hat{U} = \exp\left[\frac{\kappa}{\Delta}\left(\hat{\sigma}^+\hat{a} - \hat{\sigma}^-\hat{a}^\dagger\right)\right] \equiv \exp(\hat{A}), \tag{3.31}$$

where $\Delta = \omega_{10} - \omega_0$ is the detuning. By using the Campbell-Baker-Hausdorff lemma to the second order, we obtain

$$\begin{aligned}\hat{H}' &= \hat{U}^\dagger\hat{H}\hat{U} \approx \hat{H} + \left[\hat{H}, \hat{A}\right] + \frac{1}{2}\left[\left[\hat{H}, \hat{A}\right], \hat{A}\right] \\ &\approx -\frac{\hbar}{2}\left(\omega_{10} + \frac{\kappa^2}{\Delta}\right)\hat{\sigma}_z + \hbar\omega_0\left(\hat{a}^\dagger\hat{a} + \frac{1}{2}\right) - \hbar\frac{\kappa^2}{\Delta}\hat{\sigma}_z\hat{a}^\dagger\hat{a}.\end{aligned} \tag{3.32}$$

On the one hand, the dispersive coupling causes an ac Stark shift of the qubit transition frequency by $(2\kappa^2/\Delta)\langle\hat{a}^\dagger\hat{a}\rangle$ and a Lamb shift of it by κ^2/Δ. On the other hand, the resonator's resonant frequency is shifted by $(\kappa^2/\Delta)\hat{\sigma}_z$, which means that we can read qubit state out by probing the resonator near its bare resonant frequency ω_0 [39].

In the dispersive coupling regime, single-qubit quantum gates can be realized by driving the qubit with an extra microwave field through the resonator [31].

[3]The coupling strength κ is much larger than the resonator decay rate γ (see Sec. 2.1) and the qubit relaxation rate Γ_1 (to be introduced in the next chapter).

Several qubits can be placed in the gap between the center conductor of the CPW resonator and the ground plane, and even if two of them are spatially well separated (*e.g.* located near the two ends of the resonator), they can be coupled through virtual excitation of the resonator, as shown in Publication **I**. Details of using this type of coupling to implement universal quantum gates are also shown in Publication **I**.

4. Decoherence in Artificial Atoms

In the previous chapter, I mentioned decoherence in a CPB only very briefly. In general, decoherence of quantum superpositions (reducing of off-diagonal elements of the quantum system's density matrix) in an atom is caused by interaction between the atom and its environment. A model that describes this process is the Caldeira-Leggett model [8]. In this chapter, I will first give a quantitative description of decoherence in a superconducting artificial atom, which will be used as a theoretical tool for analyzing experimental data shown in Chapter 5 and Chapter 6. Then I will extend this single-atom decoherence model to a two-atom case and I will study a quantum phenomenon called *entanglement sudden death*.

4.1 Decoherence in a single artificial atom

We use the transmon qubit as an example. As shown in Eqs. (3.21) and (3.22), there are two control parameters, external flux $\varphi_{\rm ext}$ and gate charge q_g, for the qubit. Both of them can be noisy. Assuming that $\varphi_{\rm ext} = \varphi_{\rm dc} + \delta\varphi(t)$, $q_g = \delta q(t)$, and $d = 0$ for simplicity, the Hamiltonian is

$$\hat{H} = -\frac{1}{2}\left(\sqrt{2E_{\rm C}E_{\rm J0}\cos(\varphi_{\rm ext})} - \frac{E_{\rm C}}{4}\right)\hat{\sigma}_z + \delta q(t)\left[2E_{\rm C}^3 E_{\rm J0}\cos(\varphi_{\rm ext})\right]^{1/4}\hat{\sigma}_x. \tag{4.1}$$

Here I take $0.3\pi < \varphi_{\rm ext} < 0.4\pi$ (see Fig. 3.6), and I also rotate the coordinates around z-axis by $\pi/2$ ($\hat{\sigma}_y \to -\hat{\sigma}_x$). For small flux fluctuations $\delta\varphi(t) \approx 0$,

$$[\cos(\varphi_{\rm ext})]^{1/(2k)} \approx [\cos(\varphi_{\rm dc})]^{1/(2k)}\left[1 - \frac{\delta\varphi(t)}{2k\cos(\varphi_{\rm dc})}\right], \quad \text{where} \quad k = 1, 2. \tag{4.2}$$

Thus the Hamiltonian can be rewritten as

$$\hat{H} \approx -\frac{\hbar}{2}\left[\omega_{10} - \delta\omega(t)\right]\hat{\sigma}_z + \frac{\hbar}{2}\delta\Omega(t)\hat{\sigma}_x, \tag{4.3}$$

with

$$\hbar\omega_{10} = \sqrt{2E_{\rm C}E_{\rm J0}\cos(\varphi_{\rm dc})} - \frac{E_{\rm C}}{4}, \quad \hbar\delta\omega(t) = \delta\varphi(t)\sqrt{\frac{E_{\rm C}E_{\rm J0}}{2\cos(\varphi_{\rm dc})}}, \tag{4.4}$$

and[1]

$$\hbar\delta\Omega(t) \approx 2\delta q(t)\left[2E_{\rm C}^3 E_{\rm J0}\cos(\varphi_{\rm dc})\right]^{1/4}. \tag{4.5}$$

If we follow the same procedures as those in Eqs. (2.15 - 2.20), by rewriting the Hamiltonian Eq. (4.3) as $\hat{H} = \hat{H}_0 + \hat{H}_{\rm int}(t)$, with

$$\hat{H}_0 = -\frac{\hbar}{2}\omega_{10}\hat{\sigma}_z \ \text{ and } \ \hat{H}_{\rm int}(t) = \frac{\hbar}{2}\left[\delta\omega(t)\hat{\sigma}_z + \delta\Omega(t)\hat{\sigma}_x\right], \tag{4.6}$$

we obtain a master equation in the interaction picture

$$\begin{aligned}\dot{\tilde{\hat{\rho}}}(t) \ &\approx \ \frac{1}{8}S_\perp(\omega_{10})\left[2\hat{\sigma}^-\tilde{\hat{\rho}}(t)\hat{\sigma}^+ - \hat{\sigma}^+\hat{\sigma}^-\tilde{\hat{\rho}}(t) - \tilde{\hat{\rho}}(t)\hat{\sigma}^+\hat{\sigma}^-\right]\\ &\quad+\frac{1}{8}S_\perp(-\omega_{10})\left[2\hat{\sigma}^+\tilde{\hat{\rho}}(t)\hat{\sigma}^- - \hat{\sigma}^-\hat{\sigma}^+\tilde{\hat{\rho}}(t) - \tilde{\hat{\rho}}(t)\hat{\sigma}^-\hat{\sigma}^+\right]\\ &\quad+\frac{1}{4}S_\parallel(0)\left[\hat{\sigma}_z\tilde{\hat{\rho}}(t)\hat{\sigma}_z - \tilde{\hat{\rho}}(t)\right],\end{aligned} \tag{4.7}$$

where $S_\perp(\pm\omega_{10}) = \int_{-\infty}^{\infty} d\tau e^{\pm i\omega_{10}\tau}\langle\delta\Omega(\tau)\delta\Omega(0)\rangle$ and $S_\parallel(0) = \int_{-\infty}^{\infty} d\tau\langle\delta\omega(\tau)\delta\omega(0)\rangle$.

The right-hand side of Eq. (4.7) can be written in the matrix form as

$$\frac{1}{4}\begin{bmatrix} -S_\perp(-\omega_{10})\tilde{\rho}_{00} + S_\perp(\omega_{10})\tilde{\rho}_{11} & -\frac{1}{2}[4S_\parallel(0) + S_\perp(\omega_{10}) + S_\perp(-\omega_{10})]\tilde{\rho}_{01} \\ -\frac{1}{2}[4S_\parallel(0) + S_\perp(\omega_{10}) + S_\perp(-\omega_{10})]\tilde{\rho}_{10} & S_\perp(-\omega_{10})\tilde{\rho}_{00} - S_\perp(\omega_{10})\tilde{\rho}_{11}\end{bmatrix},$$

with $\tilde{\rho}_{jk} = \langle j|\tilde{\hat{\rho}}(t)|k\rangle$. The longitudinal ($\hat{\sigma}_z$) noise $S_\parallel(0)$ only affects the off-diagonal density matrix elements, known as pure dephasing (decoherence); while the transverse ($\hat{\sigma}_x$) noise $S_\perp(\pm\omega_{10})$ affects both the diagonal and the off-diagonal elements. Since the origin of $\delta\Omega(t)$ is the gate voltage fluctuation [see Eq. (4.5) and the definitions below Eq. (3.10)], we can then rewrite $S_\perp(\pm\omega_{10})$ as (see Sec. 2.1.1)

$$S_\perp(\omega_{10}) = \frac{2\omega_{10}R_0C_g^2}{\hbar e^2}\left[2E_{\rm C}^3E_{\rm J0}\cos(\varphi_{\rm dc})\right]^{1/2}(\bar{n}+1) \equiv 4\Gamma_1(\bar{n}+1), \tag{4.8}$$

$$S_\perp(-\omega_{10}) = \frac{2\omega_{10}R_0C_g^2}{\hbar e^2}\left[2E_{\rm C}^3E_{\rm J0}\cos(\varphi_{\rm dc})\right]^{1/2}\bar{n} \equiv 4\Gamma_1\bar{n}, \tag{4.9}$$

with $\bar{n} = \{\exp[\hbar\omega_{10}/(k_BT)] - 1\}^{-1}$ and the relaxation rate Γ_1.

By transforming Eq. (4.7) back to the Schrödinger picture, we obtain the Markov master equation for the qubit in thermal equilibrium

$$\begin{aligned}\dot{\hat{\rho}} \ &= \ -\frac{i}{\hbar}\left[\hat{H}_0,\hat{\rho}\right] + \frac{\Gamma_1}{2}(\bar{n}+1)\left(2\hat{\sigma}^-\hat{\rho}\hat{\sigma}^+ - \hat{\sigma}^+\hat{\sigma}^-\hat{\rho} - \hat{\rho}\hat{\sigma}^+\hat{\sigma}^-\right)\\ &\quad+\frac{\Gamma_1}{2}\bar{n}\left(2\hat{\sigma}^+\hat{\rho}\hat{\sigma}^- - \hat{\sigma}^-\hat{\sigma}^+\hat{\rho} - \hat{\rho}\hat{\sigma}^-\hat{\sigma}^+\right) + \frac{\Gamma_\varphi}{2}\left(\hat{\sigma}_z\hat{\rho}\hat{\sigma}_z - \hat{\rho}\right),\end{aligned} \tag{4.10}$$

with the pure dephasing rate $\Gamma_\varphi \equiv S_\parallel(0)/2$. In Lecture 2 of [13], a more systematic method to derive the master equation for a two-level atom coupled to bosonic reservoirs in thermal equilibrium is provided.

[1]Here I neglect the $\delta g(t)\delta\varphi(t)$ term since $\delta\varphi(t)/\left[2\cos(\varphi_{\rm dc})\right] \ll 1$. However it may be interesting to study decoherence via correlated noises.

In real experiments, superconducting qubits are cooled down to very low temperature, $k_BT \ll \hbar\omega_{10}$. In this limit, the excitation of the qubit by the transverse noise is negligible. So a reduced master equation [taking $\bar{n} \approx 0$ in Eq. (4.10)],

$$\dot{\hat{\rho}} \approx -\frac{i}{\hbar}\left[\hat{H}_0, \hat{\rho}\right] + \frac{1}{2}\begin{bmatrix} 2\Gamma_1\rho_{11} & -(\Gamma_1 + 2\Gamma_\varphi)\rho_{01} \\ -(\Gamma_1 + 2\Gamma_\varphi)\rho_{10} & -2\Gamma_1\rho_{11} \end{bmatrix}, \tag{4.11}$$

is commonly used for describing decoherence processes in superconducting qubits. The energy relaxation time $T_1 \equiv \Gamma_1^{-1}$, and the total decoherence time $T_2 \equiv (\Gamma_\varphi + \Gamma_1/2)^{-1} \leq 2T_1$. From now on, I will only consider the low temperature limit.

Experiments on studying decoherence of superconducting qubits [40] revealed that the energy relaxation is a spontaneous emission process induced by the Ohmic (f) high-frequency noise, and that the dephasing was dominated by the $1/f$ low-frequency noise. These results are in reasonably good agreement with what we learn from Eq. (4.7). Furthermore, the experiments in [40] also indicated the T^2 temperature dependence of the $1/f$ noise spectral density and the $\omega \sim T$ crossover between f noise and $1/f$ noise. To explain these properties, Shnirman and his co-works proposed a model [41], in which, instead of considering collective harmonic oscillators as noise sources, both f noise and $1/f$ noise were produced by one ensemble of coherent two-level system (TLS) fluctuators [42, 43].

In the presence of a coherent driving field transversely coupled to the qubit

$$\hat{H}_{\rm drive} = \hbar\Omega\cos(\omega_{\rm drive}t)\hat{\sigma}_x, \tag{4.12}$$

with Rabi frequency Ω and driving frequency $\omega_{\rm drive}$, the master equation can be written as [14]

$$\dot{\hat{\rho}} \approx -\frac{i}{\hbar}\left[\hat{H}_0 + \hat{H}_{\rm drive}, \hat{\rho}\right] + \mathcal{L}[\hat{\rho}], \tag{4.13}$$

as long as $|\Omega| \ll |\omega_{10}|$, where the Liouvillean $\mathcal{L}[\hat{\rho}]$ represents the matrix on the right-hand side of Eq. (4.11) describing the relaxation and the dephasing.

The discussion above can be easily extended to a three-level system. In Publication **VII**, the Liouvillean describing the relaxation process was derived microscopically by following [13], and the Liouvillean for pure dephasing was derived semiclassically. The master equation for the phase qutrit reads

$$\dot{\hat{\rho}} \approx -\frac{i}{\hbar}\left[\hat{H}(t), \hat{\rho}\right] + \frac{1}{2}\begin{bmatrix} 2\Gamma_{10}\rho_{11} & -\gamma_{10}\rho_{01} & -\gamma_{20}\rho_{02} \\ -\gamma_{10}\rho_{10} & -2\Gamma_{10}\rho_{11} + 2\Gamma_{21}\rho_{22} & -(\gamma_{10}+\gamma_{20})\rho_{12} \\ -\gamma_{20}\rho_{20} & -(\gamma_{10}+\gamma_{20})\rho_{21} & -2\Gamma_{21}\rho_{22} \end{bmatrix}, \tag{4.14}$$

where Γ_{jk} is the $|j\rangle \to |k\rangle$ relaxation rate, the decoherence rates $\gamma_{10} = \Gamma_{10} + \Gamma_{10}^{\varphi}$, $\gamma_{20} = \Gamma_{21} + \Gamma_{20}^{\varphi}$, and $\hat{H}(t)$ was given in Eq. (3.25).

4.2 Decoherence in a bipartite system – ESD

In a composite system of more than one quantum particle, *e.g.* two qubits (known as a bipartite system), there can be non-classical correlations between the particles. If such non-classical correlations exist, the system's state cannot be written as a convex combination of direct products of individual particles states [44]. This system is called *entangled* [28, 45]. When each qubit in the bipartite system experiences independent relaxation processes (caused by transverse zero-temperature thermal reservoir), the entanglement is destroyed abruptly (sudden death) for some entangled states [46]. Later Yu and Eberly [47] pointed out that when independent pure dephasing was added to each qubit, all initially entangled states suffered sudden death. This entanglement sudden death (ESD) phenomenon was demonstrated experimentally in 2007 [48].

We have added on-resonant continuous driving with Rabi frequency Ω_j for qubit-j ($j = A, B$) and a transverse qubit-qubit coupling with strength ω_c into the original ESD model studied by Yu and Eberly [46]. In a doubly rotating frame, the master equation for the density matrix $\hat{\rho}$ of the bipartite system reads

$$\dot{\hat{\rho}} = -\frac{i}{\hbar}\left[\hat{H}_{AB}, \hat{\rho}\right] + \sum_{j=A,B} \frac{\Gamma_j}{2}\left(2\hat{\sigma}_j^- \hat{\rho}\hat{\sigma}_j^+ - \hat{\sigma}_j^+\hat{\sigma}_j^-\hat{\rho} - \hat{\rho}\hat{\sigma}_j^+\hat{\sigma}_j^-\right), \tag{4.15}$$

with the Hamiltonian

$$\hat{H}_{AB} = \frac{\hbar}{2}\Omega_A \hat{\sigma}_x \otimes \hat{I} + \frac{\hbar}{2}\Omega_B \hat{I} \otimes \hat{\sigma}_x + \frac{\hbar}{2}\omega_c\left(\hat{\sigma}_x \otimes \hat{\sigma}_x + \hat{\sigma}_y \otimes \hat{\sigma}_y\right), \tag{4.16}$$

the energy relaxation rate Γ_j of qubit-j, and the single-qubit raising (lowering) operators $\hat{\sigma}_A^{\pm} = \hat{\sigma}^{\pm} \otimes \hat{I}$, $\hat{\sigma}_B^{\pm} = \hat{I} \otimes \hat{\sigma}^{\pm}$ ($\hat{I}$ the Identity operator).

4.2.1 Secular limit

In Publications **II** and **IV**, we studied the ESD in the secular driving limit $\Omega_j \gg \Gamma_j$ [37]. In this limit, the master equation (4.15) can be analytically solved for the so-called "X"-states

$$\hat{\rho}(t) = \begin{bmatrix} a(t) & 0 & 0 & w(t) \\ 0 & b(t) & z(t) & 0 \\ 0 & z^*(t) & c(t) & 0 \\ w^*(t) & 0 & 0 & d(t) \end{bmatrix}. \tag{4.17}$$

A measure of entanglement, the concurrence $\mathcal{C}[\hat{\rho}]$ [49], is calculated in the time domain for two sets of initially entangled "X"-states, the *Werner* states $\hat{\rho}_W$ [44] and

the Yu-Eberly (*YE*) states $\hat{\rho}_{YE}$ [46], respectively, where

$$\hat{\rho}_W = \frac{1}{3}\begin{bmatrix} 1-f & 0 & 0 & 0 \\ 0 & (1+2f)/2 & (1-4f)/2 & 0 \\ 0 & (1-4f)/2 & (1+2f)/2 & 0 \\ 0 & 0 & 0 & 1-f \end{bmatrix}, \tag{4.18}$$

$$\hat{\rho}_{YE} = \frac{1}{3}\begin{bmatrix} 1-\alpha & 0 & 0 & 0 \\ 0 & 1 & 1 & 0 \\ 0 & 1 & 1 & 0 \\ 0 & 0 & 0 & \alpha \end{bmatrix}, \tag{4.19}$$

with $0.25 \leq f \leq 1$ and $0 \leq \alpha \leq 1$.

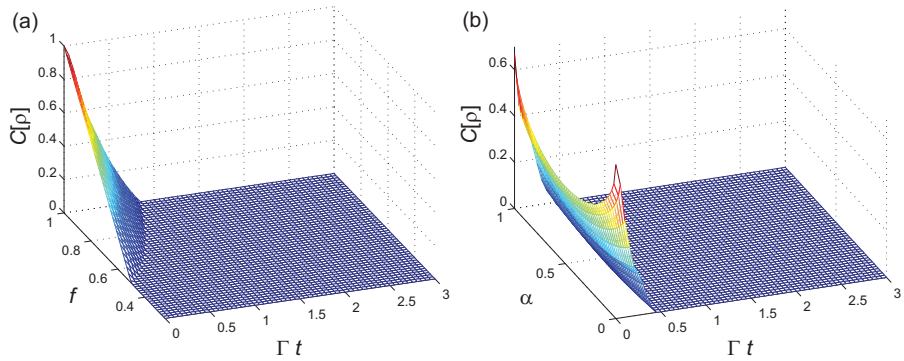

Figure 4.1. Time evolution of the concurrence under coherent driving for (a) *Werner* state and (b) *YE* state. Here we assume $\Gamma_A = \Gamma_B \equiv \Gamma$ and $\Omega_A = \Omega_B \equiv \Omega$ for simplicity, and take $\omega_c = 5\Gamma$, $\Omega = 25\Gamma$.

In the case of no driving and no qubit-qubit coupling studied by Yu and Eberly, the entanglement of *YE* states with $\alpha < 1/3$ [46] and that of *Werner* states with $f > 0.714$ [50] decay asymptotically. As shown in Fig. 4.1, the concurrences in the whole range of f and α disappear abruptly in the case of secular driving and qubit-qubit coupling. These differences are mainly caused by the raising of reservoirs' effective temperature and the appearing of effective pure dephasing due to the drivings (see Publication **II**). The time evolution of *Werner* states are independent of the qubit-qubit coupling ω_c, however, as studied in Publication **IV**, for other "X"-states the ESD behaviors are dependent on ω_c, and the entanglement can be regenerated after sudden death. This is due to the fact that the transverse (*XY*) qubit-qubit coupling can produce perfect entanglers [51, 52] and can generate maximum entanglement from disentangled states in a period proportional to $2\pi/\omega_c$ (see Sec. IV of Publication **I**).

4.2.2 Non-secular limit

In the non-secular limit where Ω is comparable to Γ, by numerically solving Eq. (4.15) with parameters $\omega_c = 5\Gamma$ and $\Omega = \Gamma$, the time dependent concurrence for *Werner* states are calculated and plotted in Fig. 4.2(a). Shortly after the ESD, entanglement is regenerated via the *XY* coupling, and it seems to have long life time and be independent on the initial states. In Publication **V**, we found the steady-state concurrence at time $t \to \infty$ analytically,

$$\mathcal{C}^{(\infty)}[\hat{\rho}] = \max\left\{\frac{2\Omega^2(2\omega_c\Gamma - \Omega^2)}{(\Gamma^2 + 2\Omega^2)^2 + 4\omega_c^2\Gamma^2}, 0\right\}, \tag{4.20}$$

as plotted in Fig. 4.2(b).

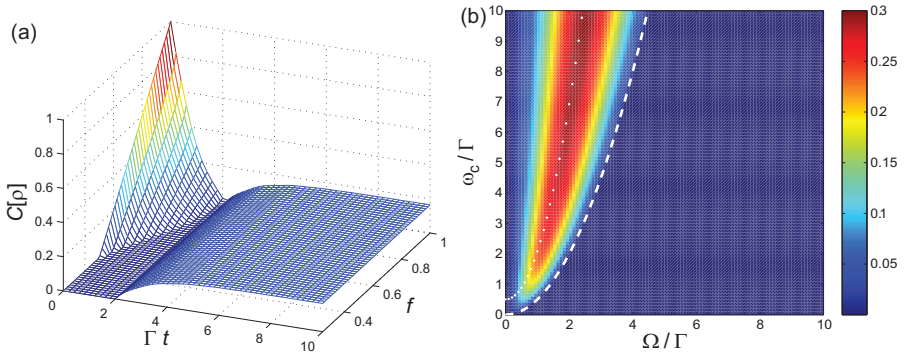

Figure 4.2. (a) Time evolution of the concurrence for the *Werner* state with $\omega_c = 5\Gamma$, $\Omega = \Gamma$. (b) The steady-state concurrence as a function of ω_c and Ω.

The solution (steady state) of Eq. (4.15), $\hat{\rho}(\infty)$, is independent of the initial state $\hat{\rho}(0)$, and so it is the concurrence $\mathcal{C}^{(\infty)}[\hat{\rho}]$. From Eq. (4.20), one can easily find out that the boundary between the region of finite entanglement and that of no entanglement is a parabola, $\omega_c = \Omega^2/(2\Gamma)$, as illustrated by the dashed line in Fig. 4.2(b). The steady-state concurrence reaches the maximum value of

$$\mathcal{C}^{(\infty)}_{\max} = \frac{\Omega^2}{\Omega^2 + \sqrt{\Omega^4 + (\Gamma^2 + 2\Omega^2)^2}} \quad \text{at} \quad \omega_c = \frac{\Omega^2}{2\Gamma} + \frac{\sqrt{\Omega^4 + (\Gamma^2 + 2\Omega^2)^2}}{2\Gamma},$$

as illustrated by the dotted line in Fig. 4.2(b).

Since this steady-state entanglement is robust under decoherence, independent of the initial state of the qubits, and relatively easy to generate, such bipartite systems could be used as “entanglement batteries”. A protocol of using simple local unitary operations to harvest and transmit the steady-state entanglement in a quantum circuit consisting of qubits and resonators was suggested in Publication **V**.

5. The Autler-Townes Effect in a Phase Qutrit

As derived in Publication **VII**, the energy levels in a superconducting phase qutrit form a *ladder* (also called *cascade*) configuration, in which only the transitions between adjacent energy levels are dipole allowed.

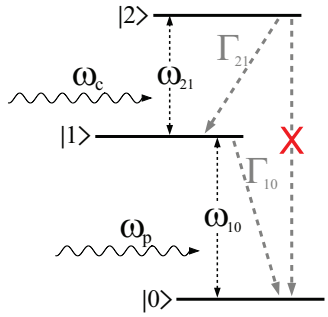

Figure 5.1. A ladder three-level atom is irradiated by two single-mode electromagnetic fields of frequency $\omega_{\rm p}$ and $\omega_{\rm c}$. $\omega_{j,j-1}$ denotes the transition frequency between atomic levels $|j\rangle$ and $|j-1\rangle$, and $\Gamma_{j,j-1}$ the spontaneous decay rate from $|j\rangle$ to $|j-1\rangle$. The spontaneous decay from $|2\rangle$ to $|0\rangle$ is approximately dipole forbidden.

As shown in Fig. 5.1, the ground level $|0\rangle$ is coupled to the intermediate level $|1\rangle$ by a monochromatic *probe* field of angular frequency $\omega_{\rm p}$, while the upper level $|2\rangle$ and the intermediate level $|1\rangle$ are coupled by another monochromatic *coupling* field of angular frequency $\omega_{\rm c}$.

5.1 The Autler-Townes effect in the dressed-atom picture

Let us first ignore the probe field ω_p, and ignore the interaction between the qutrit and the coupling field ω_c. The Hamiltonian of the qutrit reads

$$\hat{H}_{\rm atom} = \hbar\left[\omega_{10}|1\rangle\langle 1| + (\omega_{10}+\omega_{21})|2\rangle\langle 2|\right], \tag{5.1}$$

and the Hamiltonian of the coupling field

$$\hat{H}_{\rm coup} = \hbar\omega_{\rm c}\left(\hat{a}^{\dagger}\hat{a} + 1/2\right), \tag{5.2}$$

with $\hat{a}^{\dagger}$ ($\hat{a}$) the photon creation (annihilation) operator.

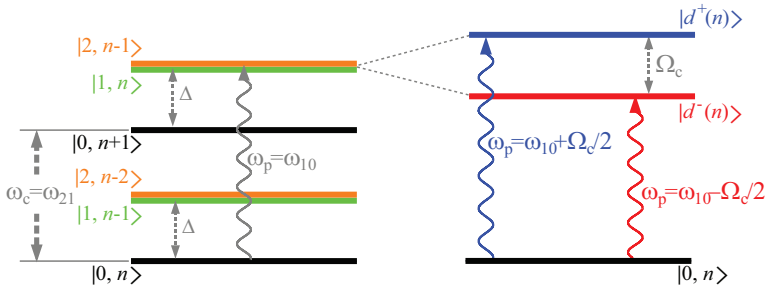

Figure 5.2. Energy diagram of the Autler-Townes splitting. The coupling tone and the two upper levels of the three-level system form dressed states.

On the left-hand side of Fig. 5.2, the manifolds of unperturbed *atom+coupling field* states

$$\mathcal{E}(n-1) = \{|0,n\rangle, |1,n-1\rangle, |2,n-2\rangle\},$$
$$\mathcal{E}(n) = \{|0,n+1\rangle, |1,n\rangle, |2,n-1\rangle\}$$

are shown. Here $|j,n\rangle = |j\rangle \otimes |n\rangle$ ($j = 0,1,2$), n and $|n\rangle$ are the eigenvalue and corresponding eigenvector of the photon number operator $\hat{a}^{\dagger}\hat{a}$. For simplicity, we assume that the coupling field is on resonant with the atomic $|1\rangle \leftrightarrow |2\rangle$ transition, $\omega_{\rm c} = \omega_{21}$, so that the levels $|2,n-1\rangle$ and $|1,n\rangle$ have the same energy. The detuning between the atomic $|0\rangle \leftrightarrow |1\rangle$ transition frequency and the coupling field frequency is defined as $\Delta \equiv \omega_{10} - \omega_{\rm c}$. At very low temperature, $k_B T \ll \hbar\omega_{10}, \hbar\omega_{21}$, the *atom+coupling field* system is prepared in the state $|0,n\rangle$, and it can be excited to $|1,n\rangle$ if the probe field is switched on and tuned to near resonant with $|0\rangle \leftrightarrow |1\rangle$ transition, $\omega_{\rm p} \approx \omega_{10}$.

Now by introducing an interaction,

$$\hat{H}_{\rm int} = \hbar g\left(\hat{a}^{\dagger}|1\rangle\langle 2| + \hat{a}|2\rangle\langle 1|\right), \tag{5.3}$$

between the coupling field and the atom, with dipole interacting constant g, the two degenerate levels $|1,n\rangle$ and $|2,n-1\rangle$ form dressed levels [37]

$$|d^{+}(n)\rangle = \frac{1}{\sqrt{2}}\left(|1,n\rangle + |2,n-1\rangle\right) \quad \text{and} \quad |d^{-}(n)\rangle = \frac{1}{\sqrt{2}}\left(|1,n\rangle - |2,n-1\rangle\right) \tag{5.4}$$

separated by a Rabi frequency $\Omega_{\rm c} = 2g\sqrt{n+1}$ (shown on the right-hand side of Fig. 5.2). Since both dressed levels contain equal amounts of $|1,n\rangle$, the two transitions

$|0,n\rangle \rightarrow |d^+(n)\rangle$ and $|0,n\rangle \rightarrow |d^-(n)\rangle$ (as indicated by the blue and red wavy arrows, respectively, in Fig. 5.2) are allowed with the same probability for the probe field at frequency $\omega_\mathrm{p} \approx \omega_{10} \pm \Omega_\mathrm{c}/2$. The absorption spectrum of the probe field (as well as the occupation probability of level $|1\rangle$) splits into two Lorentzians with a separation Ω_c, known as the *Autler-Townes splitting* or *Autler-Townes doublet*.

5.2 The Autler-Townes effect in a phase qutrit

From the simple dressed-atom interpretation given in the previous section, one would expect that the Autler-Townes doublet is symmetric with respect to ω_{10} [as indicated by the (green) dashed lines in Fig. 5.3, obtained by analytically solving the three-level master equation in a doubly rotating frame (see the following discussions)]. In the spectroscopy measurements we kept the coupling field on-resonant with $|1\rangle \leftrightarrow |2\rangle$ transition, and measured the population P_1 of level $|1\rangle$ at different probe frequencies ω_p. However, as indicated by the solid lines in Fig. 5.3, asymmetric splittings of the population P_1 were observed in the experiment.

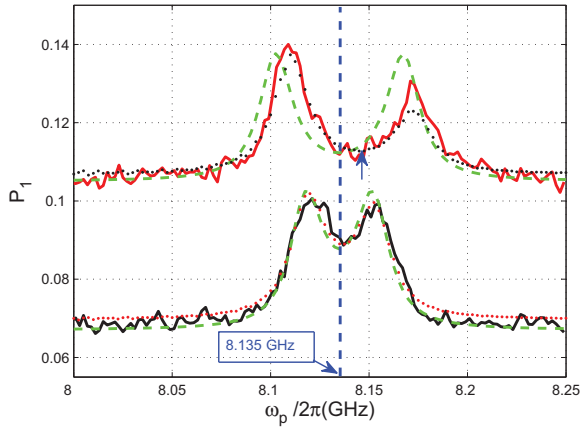

Figure 5.3. Autler-Townes splittings in a phase qubit, taken from Fig. 4 of Publication **VII**. The solid curves are the population P_1 measured at $\Omega_\mathrm{c}/2\pi = 36$ MHz (black) and $\Omega_\mathrm{c}/2\pi = 66$ MHz (red). The dashed (green) curves are plotted by using Eq. (5.9). The dotted curves are plotted by numerically solving a five-level master equation based on Eq. (5.6). The vertical (blue) dashed line indicates the $|0\rangle \leftrightarrow |1\rangle$ transition frequency $\omega_{10} = 2\pi \times 8.135$ GHz.

To understand this difference between the experiment and the theory, we need to re-consider the interaction Hamiltonian H_int more carefully. At the beginning of this chapter (see Fig. 5.1), we assumed that each electromagnetic field drives only one transition. This assumption has been successfully adopted in conventional

quantum optics to study phenomena involving multi-level atom, such as electromagnetically induced transparency (EIT) [53]. It is not valid here since unlike in natural atoms, the anharmonicity in a superconducting qutrit is small, which means that when the coupling field is on resonant with the $|1\rangle \leftrightarrow |2\rangle$ transition it is also near resonant with the $|0\rangle \leftrightarrow |1\rangle$ transition, and so is the probe field. To fully describe the couplings, as well as the qutrit, we use the Hamiltonian shown in Eq. (3.25),

$$\hat{H}(t) \approx \hbar \begin{bmatrix} 0 & 0.69g(t) & 0.02g(t) \\ 0.69g(t) & \omega_{10} & g(t) \\ 0.02g(t) & \Omega(t) & \omega_{10}+\omega_{21} \end{bmatrix}, \tag{5.5}$$

with $g(t) = g_\mathrm{c}\cos(\omega_\mathrm{c}t) + g_\mathrm{p}\cos(\omega_\mathrm{p}t)$. Here we assume the electromagnetic fields are classical. By taking the energy relaxations and pure dephasings into account, the dynamics of the qutrit is governed by the master equation (see Sec. 4.1)

$$\dot{\hat{\rho}} \approx -\frac{i}{\hbar}\left[\hat{H}(t), \hat{\rho}\right] + \frac{1}{2}\begin{bmatrix} 2\Gamma_{10}\rho_{11} & -\gamma_{10}\rho_{01} & -\gamma_{20}\rho_{02} \\ -\gamma_{10}\rho_{10} & -2\Gamma_{10}\rho_{11} + 2\Gamma_{21}\rho_{22} & -(\gamma_{10}+\gamma_{20})\rho_{12} \\ -\gamma_{20}\rho_{20} & -(\gamma_{10}+\gamma_{20})\rho_{21} & -2\Gamma_{21}\rho_{22} \end{bmatrix}. \tag{5.6}$$

The steady-state solution of the master equation above can be obtained analytically in a doubly rotating frame (of frequencies ω_p and $\omega_\mathrm{p}+\omega_\mathrm{c}$). In this doubly rotating frame, Eq. (5.5) takes the form (the time-dependent terms are neglected, see Sec. III of Publication **VII**)

$$\hat{\tilde{H}} \approx \hbar \begin{bmatrix} 0 & \Omega_\mathrm{p}/2 & 0 \\ \Omega_\mathrm{p}/2 & \Delta_\mathrm{p} & \Omega_\mathrm{c}/2 \\ 0 & \Omega_\mathrm{c}/2 & \Delta_\mathrm{p}+\Delta_\mathrm{c} \end{bmatrix}, \tag{5.7}$$

with the Rabi frequencies $\Omega_\mathrm{p} = 0.69g_\mathrm{p}$, $\Omega_\mathrm{c} = g_\mathrm{c}$, and the detunings $\Delta_\mathrm{p} = \omega_{10} - \omega_\mathrm{p}$, $\Delta_\mathrm{c} = \omega_{21} - \omega_\mathrm{c}$. The dissipation terms in Eq. (5.6) remain the same in the doubly rotating frame. Then the steady state ($t \to \infty$) is calculated by solving the equation

$$-\frac{i}{\hbar}\left[\hat{\tilde{H}}, \hat{\tilde{\rho}}\right] + \frac{1}{2}\begin{bmatrix} 2\Gamma_{10}\tilde{\rho}_{11} & -\gamma_{10}\tilde{\rho}_{01} & -\gamma_{20}\tilde{\rho}_{02} \\ -\gamma_{10}\tilde{\rho}_{10} & -2\Gamma_{10}\tilde{\rho}_{11} + 2\Gamma_{21}\tilde{\rho}_{22} & -(\gamma_{10}+\gamma_{20})\tilde{\rho}_{12} \\ -\gamma_{20}\tilde{\rho}_{20} & -(\gamma_{10}+\gamma_{20})\tilde{\rho}_{21} & -2\Gamma_{21}\tilde{\rho}_{22} \end{bmatrix} = 0, \tag{5.8}$$

where $\hat{\tilde{\rho}}$ is the density matrix in the doubly rotating frame.

In the steady state, the occupation probability of level $|1\rangle$ is approximately

$$P_1 = \tilde{\rho}_{11}(\infty) \approx \frac{\Omega_\mathrm{p}^2\left[4\Delta_\mathrm{p}^2\gamma_{10} + \gamma_{20}(\Omega_\mathrm{c}^2 + \gamma_{10}\gamma_{20})\right]}{\Gamma_{10}\left[16\Delta_\mathrm{p}^4 + (\Omega_\mathrm{c}^2 + \gamma_{10}\gamma_{20})^2 + 4\Delta_\mathrm{p}^2(\gamma_{10}^2 + \gamma_{20}^2 - 2\Omega_\mathrm{c}^2)\right]}, \tag{5.9}$$

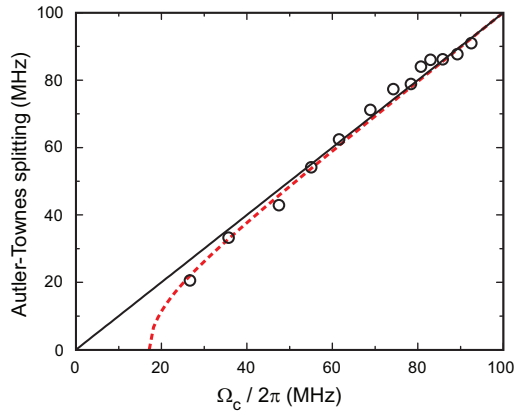

Figure 5.4. The Autler-Townes doublet separation versus the Rabi frequency Ω_c, taken from Fig. 5 of Publication **VII**. The circles are the experimental results, the solid straight line is the prediction of the dressed-atom picture (without decoherence), and the (red) dotted curve is from Eq. (5.10).

which is plotted in Fig. 5.3 (the greed dashed curves). From this steady-state occupation probability P_1, we can also estimate the Autler-Townes doublet separation (see also Sec. VI of Publication **VII**),

$$\delta\omega_{\rm AT} = \sqrt{\left[\Omega_{\rm c}(\gamma_{10}+\gamma_{20})\sqrt{\Omega_{\rm c}^2+\gamma_{10}\gamma_{20}} - \gamma_{20}(\Omega_{\rm c}^2+\gamma_{10}\gamma_{20})\right]\Big/\,\gamma_{10}}. \tag{5.10}$$

As shown in Fig. 5.4, the separation given by Eq. (5.10) (the red dotted line) is not the same as the prediction by the dressed-atom model (the black solid line) discussed in Sec. 5.1. It indicates that the decoherence tends to move the Autler-Townes doublet separation away from the linear dependence of the Rabi frequency $\Omega_{\rm c}$ when $\Omega_{\rm c}$ is not much larger than the decoherence rates (non-secular limit).

In Fig. 5.3, the dotted curves were obtained by numerically solving a five-level[1] master equation generalized from the three-level master equation Eq. (5.6), and fitted the experimental data very well. However, the spectroscopy measurements only reveal the steady-state properties of the Autler-Townes effect. In order to understand the dynamics of the Autler-Townes effect, time-domain measurements were also done. In these measurements, the probe field is still continuous and near resonant with ω_{10}, but the coupling field (on resonant with ω_{21}) is pulsed, as illustrated by the insets in Fig. 5.5. The measurement pulse is applied after a varying measurement delay time. The numerical simulations for the time-domain measurements are done by solving the master equation Eq. (5.6). As indicated by

[1]The two extra levels are used to compute the leakage from $|2\rangle$ to higher energy levels, see Publication **VII**.

Fig. 5.5, the measured population shows clearly the dynamical process of formation of the Autler-Townes doublet, how it reaches the steady state and how the doublet finally collapses into a single spectroscopic peak at ω_{10} after the coupling field is switched off, and the numerical simulation results are in good agreement with the measured population. More discussions and experimental details about the Autler-Townes effect in the phase qutrit can be found in Publications **VI**, **VII** and **VIII**.

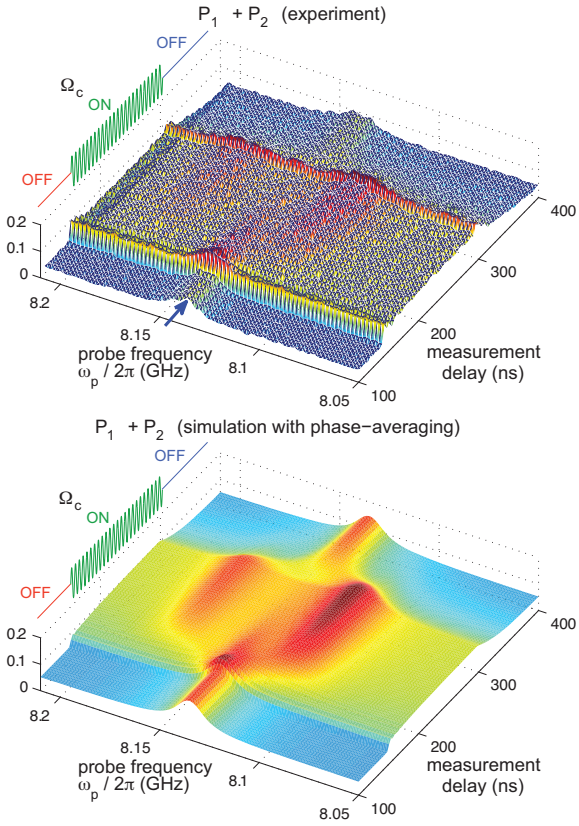

Figure 5.5. Autler-Townes splittings in the time domain. The probe field is continuously on and its frequency is swept around the qutrit's $|0\rangle \leftrightarrow |1\rangle$ transition frequency. The coupling field is on resonant with the qutrit's $|1\rangle \leftrightarrow |2\rangle$ transition, and its amplitude Ω_c is pulsed as indicated by the inset in the upper left corner.

6. Simulating Motional Averaging in a Transmon

In a schematic picture of nuclear magnetic resonance (NMR) in porous media, as shown in Fig. 6.1(b), the single pore may be divided into two areas: the surface (gray) area in which the externally applied magnetic field is modified by the pore wall, and the core (white) area in which the externally applied magnetic field is not modified. Static particles (molecules with spin-$1/2$ nuclei) in different areas can be described by two Hamiltonians $\hat{H}_1 = -\hbar\omega_1\hat{\sigma}_z/2$ and $\hat{H}_2 = -\hbar\omega_2\hat{\sigma}_z/2$, corresponding to the two different local magnetic fields, respectively. Their spectra are just two Lorentzian peaks at frequencies ω_1 and ω_2, respectively. But, randomly moving particles observe temporally short-lived variations of the magnetic field. Each single moving particle's transition frequency experiences a random telegraph noise (RTN) trajectory as shown in Fig. 6.1(a). For each single moving particle, the Hamiltonian reads

$$\hat{H}(t) = -\frac{\hbar}{2}\left[\omega_0 + \xi(t)\right]\hat{\sigma}_z. \tag{6.1}$$

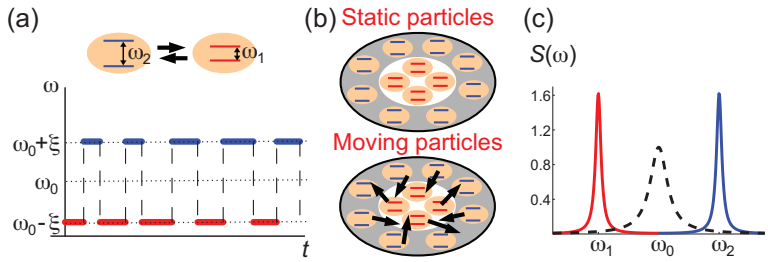

Figure 6.1. Schematics of the motional averaging. (a) A sample trajectory of the qubit transition frequency $\omega_0 + \xi(t)$. (b) A illustration of NMR pore experiment with static and moving particles. White and gray areas denote different magnetic (chemical) environments producing the the transition frequencies $\omega_1 = \omega_0 - \xi$ and $\omega_2 = \omega_0 + \xi$, respectively. (c) The spectrum of motional averaging. The solid lines denote the schematic spectra of static particles in different areas, and the dashed line corresponds to the spectrum of moving particles.

Depending on the mean rate χ of jumping from one area to the other, the spec-

trum of the ensemble of particles takes the form [54]

$$S(\omega) = \frac{4\xi^2\chi}{(\omega-\omega_0)^4 + \xi^4 + 2(\omega-\omega_0)^2(2\chi^2-\xi^2)}. \tag{6.2}$$

At low jumping rate $\chi \ll \xi$, Eq. (6.2) represents two Lorentzians with linewidth χ centered at $\omega = \omega_0 \pm \xi$, as indicated by the solid curves in Fig. 6.1(c); whereas when $\chi \gg \xi$, the two Lorentzians merge (motionally average) into one with linewidth $\xi^2/(2\chi)$ centered at $\omega = \omega_0$, as indicated by the dashed curve in Fig. 6.1(c). This phenomenon is known as the *motional averaging*.

The motional averaging has been experimentally studied in assemblies of large numbers of particles, such as in proton NMR [55] and in optically trapped cold atoms [56]. In these experiments, both ensemble averaging and time averaging have been used to obtain the spectra. In principle the same effect should be observed even at the single particle level, since the RTN jumping is a stationary Markov process [54, 57]. Experimentally, this will be hard to realize in NMR or trapped cold atoms. Nevertheless, we can simulate it with a quantum circuit consisting of just one qubit.

As shown in Sec. 4.1, when an external flux $\varphi_{\rm ext}(t) = \varphi_{\rm dc} + \varphi_{\rm mod}(t)$ is applied to the transmon qubit, its Hamiltonian can be written in the same form as Eq. (6.1)[1], with the constant transition frequency $\omega_0 = \left[\sqrt{2E_{\rm C}E_{\rm J0}\cos(\varphi_{\rm dc})} - E_{\rm C}/4\right]/\hbar$, and the modulation of transition frequency $\xi(t) = \varphi_{\rm mod}(t)\ \sqrt{E_{\rm C}E_{\rm J0}/\left[2\cos(\varphi_{\rm dc})\right]}/\hbar$. In this chapter, I will discuss the recent experiment of simulating motional averaging in a transmon qubit done in our group.

Since the pure dephasing process that occur in the dynamics of a superconducting qubit is dominated by $1/f$ noise longitudinally coupled to the qubit, this experiment is also helpful for understanding the pure dephasing in the qubit. Observations of RTN in small devices such as metal-oxide-semiconductor-field-effect transistors (MOSFETs) suggest that the charge carriers trapped in defect sites [also known as two-level system (TLS) fluctuators] located in the insulator layer of the device are possible microscopic origins of the $1/f$ noise in these devices. A summation of an ensemble of RTNs can produce $1/f$ noise [41, 57]. The Hamiltonian Eq. (6.1) also simulates the qubit longitudinally coupled to a randomly flipping TLS.

[1]Here the same notations as those in Publication **X** are used, so ω_0 is no longer the resonant frequency of the resonator.

6.1 Experimental setup

The transmon sample used for simulating single particle motional averaging is very similar to the one shown in Fig. 3.5(a). It is mounted on a printed circuit board (PCB) inside a copper sample box, as illustrated by the bottom-right inset of Fig. 6.2. The sample box is covered by an Amuneal Amumetal 4K (A4K) cryogenic magnetic shield, mounted at the mixing chamber of a dilution refrigerator, and cooled down to ~ 30 mK. The vacuum can is covered by a layer of ~ 1 mm thick Pb, which is superconducting at liquid-Helium temperature (4.2 K). A combination of superconducting shield and A4K shield provides a reasonably stable *dc* magnetic environment for the sample.

In Fig. 6.2, the wiring of the dilution refrigerator is shown. From room temperature to 4.2 K, relatively lossy cupronickel [both inner and outer conductors (I/O)] semi-rigid coaxial cables are used. From the still, Niobium semi-rigid coaxial cables are used to reduce heat load to the mixing chamber. The input line (cavity in) for sending in the probe signal of the $\lambda/4$ resonator is heavily attenuated at different temperature stages (cable loss plus attenuators ~ 60 dB). On the output line (cavity out), an extra Raditek circulator is used to block noise flowing back to the sample, and a cold amplifier (~ 30 dB gain) is located at 4.2 K. Since the flux bias line is used for both RTN modulations and *dc* bias, there is a trade-off between pulse shape distortion and thermal noise attenuation. Attenuator can not be used at mixing chamber for the flux bias line, since the attenuator may heat the mixing chamber up when the *dc* current passes through it. Normally, a powder filter is used to attenuate the thermal noise at radio frequencies and let *dc* signal passing through it. However, here we need ~ 500 MHz bandwidth for the modulation, which is much higher than the cutoff of our powder filter. We put a Mini-Circuits VLF-1000 (*dc* to 1000 MHz) low pass filter on flux bias line at the mixing chamber, and put a Mini-Circuits VLFX-500 (*dc* to 500 MHz) low pass filter at room temperature (see Fig. 6.3).

The electronic setup at room temperature is illustrated by Fig. 6.3. The *dc* flux bias and RTN modulation are generated by an Agilent 81150A arbitrary waveform generator (AWG). A continuous signal from an Agilent E8257D analog signal generator is used for driving the qubit. A continuous signal from an Agilent N5230C PNA-L network analyzer is used to probe the cavity. These two signals are combined together by a Mini-Circuits ZFSC-2-10G power splitter/combiner and sent to the cavity input line of the dilution refrigerator. The signal from the cavity output

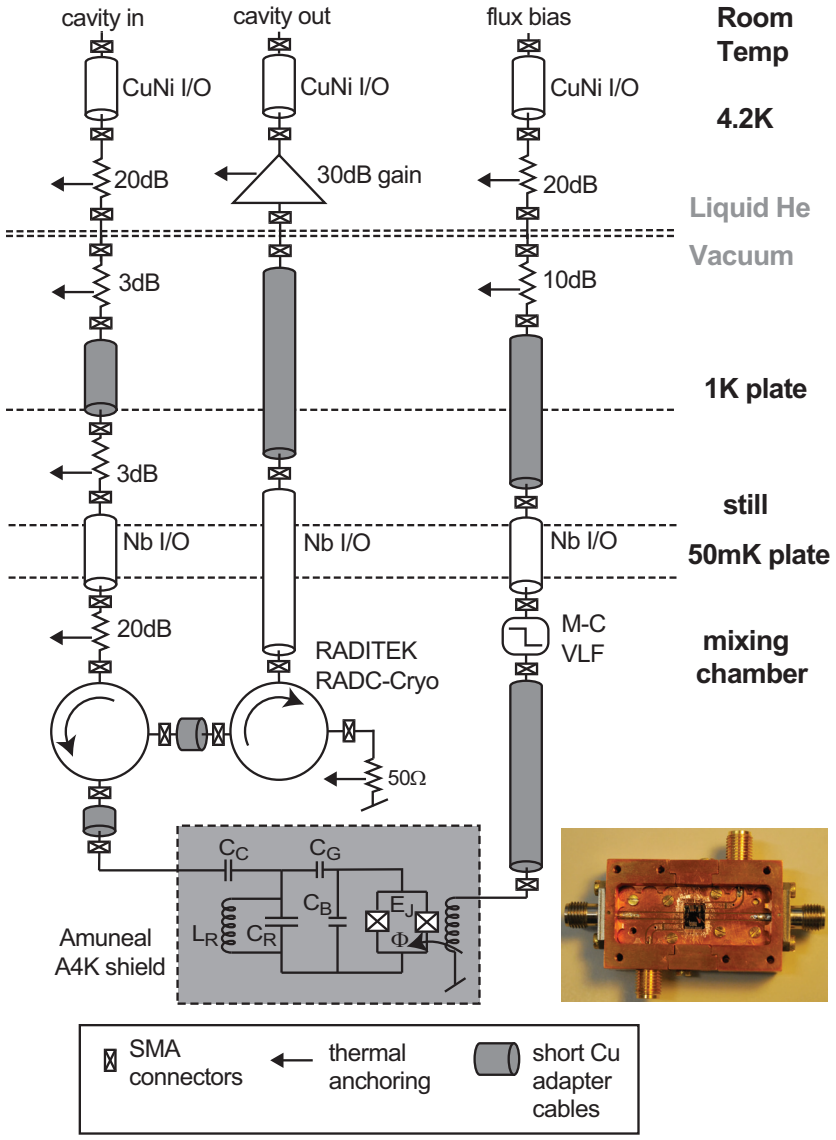

Figure 6.2. Schematics of the dilution refrigerator wiring.

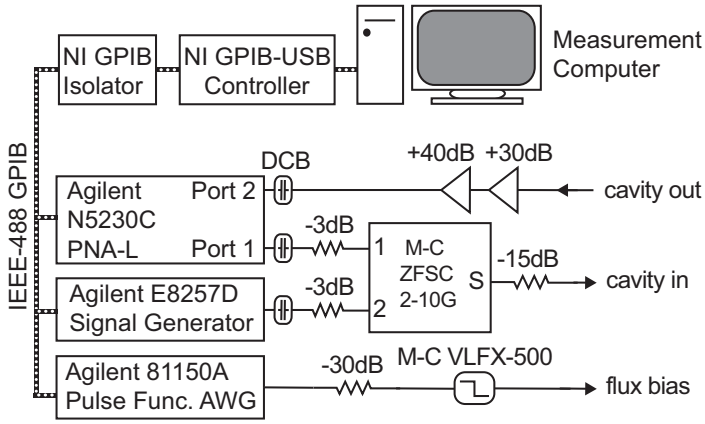

Figure 6.3. Diagram of room temperature electronics.

line of the dilution refrigerator is further amplified ($\sim$ 70 dB gain) and detected by the PNA-L network analyzer. Between the radio frequency instruments (the analog signal generator and the network analyzer) and their corresponding lines, *dc* blocks (DCBs) are used for breaking possible ground loops. All instruments are synchronized with a Stanford Research Systems (SRS) FS725 Rubidium frequency standard which is not shown in the figure. Measurement control and data processing are done by MATLAB running on a measurement computer. Communications between the measurement computer and the instruments are realized through IEEE-488 GPIB buses.

The RTN process obeys the Poisson distribution, which means that if the mean jumping frequency is χ, in a period of time t the probability of occurring n jumps is

$$P_n(t) = (\chi t)^n e^{-\chi t}/n!. \tag{6.3}$$

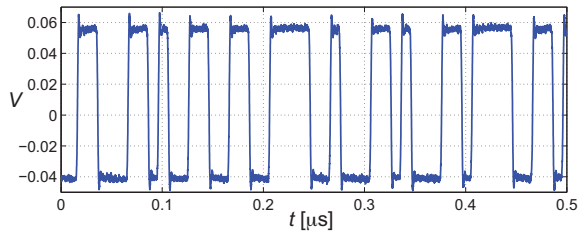

Figure 6.4. An example of RTN modulation sequence generated by the AWG at a clock frequency $\nu = 10$ KHz, taken by an oscilloscope.

To generate such pulse sequences for modulating the transition frequency of the qubit, we use MATLAB's internal Poisson random number generator $poissrnd$ to generate binary RTN sequences, and load the sequences to the Agilent 81150A

AWG. Each binary RTN sequence consists of 50000 data points and around 5000 random jumps in average. The mean jumping rate χ (of AWG's output) is modulated by changing the clock frequency ν of the AWG: $\chi \approx 5000 \times \nu$. To verify this relation between χ and ν, we observe the RTN sequences at different ν by a fast oscilloscope (10 GS/s), count the number n of edges (jumping events) for certain period of time t, and calculate the real mean jumping rate by its original definition, $\chi = n/t$. As an example, a 0.5 μs long RTN sequence with estimated mean jumping rate $\chi \approx 5000 \times 10$ KHz $= 50$ MHz is shown in Fig. 6.4. 25 jumps are counted during this 0.5 μs, which gives $\chi = 50$ MHz. As long as $\nu < 100$ KHz, the formula $\chi \approx 5000 \times \nu$ gives good estimation of mean jumping rate. For $\nu > 100$ KHz, the real mean jumping rate is smaller than the estimated one, due to the intrinsic ~ 2 ns rise/fall time of the AWG[2].

6.2 Results

The resonant frequency of the CPW resonator is $\omega_{\rm r}/2\pi = 3.795$ GHz, and the transmon qubit's transition frequency (without modulation) is set at $\omega_0/2\pi \approx 2.62$ GHz (see also Fig. 3.6). The relaxation rate $\Gamma_1 \approx 2\pi \times 1$ MHz and the decoherence rate $\Gamma_2 = \Gamma_\varphi + \Gamma_1/2 \approx 2\pi \times 3$ MHz of this qubit[3] are extracted from the numerical fittings of the Rabi oscillation data and the spectroscopy data taken without any modulation.

In our motional averaging measurements, we recorded the steady-state population $P_{\rm e}$ of the qubit's excited state at different driving frequencies (ω) and different mean jumping rates (χ) for several RTN jumping amplitudes (ξ), by probing the CPW resonator (see discussions in Sec. 3.4). In Fig. 6.5(a), the experimental $P_{\rm e}$ data for $\xi/2\pi \approx 71$ MHz is shown. The experimental data indeed reveals the motional averaging behaviors described by the spectrum $S(\omega)$ presented in Eq. (6.2). We also simulated $P_{\rm e}$ by numerically solving the master equation

$$\dot{\hat{\rho}} \approx -\frac{i}{\hbar}\left[\hat{H}_{\rm T}(t), \hat{\rho}\right] + \frac{1}{2}\begin{bmatrix} 2\Gamma_1\rho_{11} & -(\Gamma_1 + 2\Gamma_\varphi)\rho_{01} \\ -(\Gamma_1 + 2\Gamma_\varphi)\rho_{10} & -2\Gamma_1\rho_{11} \end{bmatrix}, \tag{6.4}$$

with the total Hamiltonian $\hat{H}_{\rm T}(t) = \hat{H}(t) + \hat{H}_{\rm drive}(t)$, where $\hat{H}(t)$, as given in

[2]From the datasheet of the Agilent 81150A AWG, the minimum rise/fall time is 2.5 ns. However, by checking the RTN pulses with the oscilloscope, we found that the minimum rise/fall time is slightly smaller than that.

[3]Here Γ_1 and Γ_2 are the residual relaxation rate and decoherence rate, respectively. They can be caused by the spontaneous emission of the qubit, naturally formed TLSs in the sample, *etc.*, but not the modulation.

Eq. (6.1), contains the RTN modulation $\xi(t)$, and $\hat{H}_{\rm drive}(t) = \hbar g \cos(\omega t)\hat{\sigma}_x$ is the driving term for exciting the qubit. $P_{\rm e}$ is just the diagonal element ρ_{11} of the qubit's density matrix $\hat{\rho}$. The simulation results are shown in Fig. 6.5(b). They look noisy, since for each data point, $P_{\rm e}$ is averaged over only 10 RTN sequences, much less than the number of averages for those in Fig. 2a of Publication **X**.

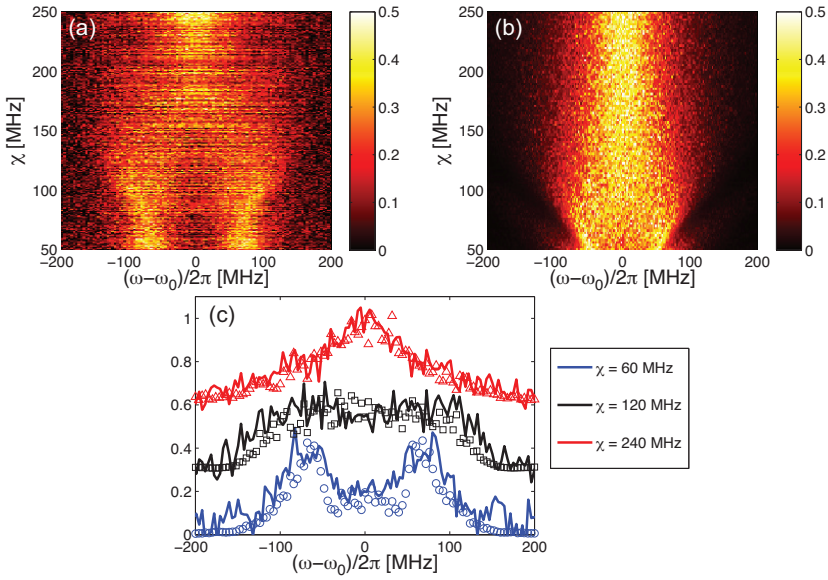

Figure 6.5. (a) Measured excited state population $P_{\rm e}$ under the RTN modulation. (b) Simulated $P_{\rm e}$ obtained by numerically solving the master equation Eq. (6.4). (c) Horizontal cuts of the measured population at $\chi = 60$ MHz (blue), $\chi = 120$ MHz (black) and $\chi = 240$ MHz (red). The base levels of $P_{\rm e}$ at $\chi = 120$ MHz and at $\chi = 240$ MHz are artificially raised by 0.3 and 0.6, respectively. The open markers indicate the corresponding results of the numerical simulation. The other parameters are $\xi/2\pi = 71$ MHz, $g/2\pi = 9$ MHz, $\Gamma_1/2\pi = 1$ MHz, and $\Gamma_2/2\pi = 3$ MHz.

Two limiting cases of the motional averaging can be found. In the case of slow jumping $\chi \ll \xi$, Eq. (6.2) is approximately

$$S(\omega) \approx \frac{2\chi}{(\omega - \omega_0 \pm \xi)^2 + \chi^2}, \tag{6.5}$$

which means that the qubit absorbs energy at $\omega_0 \pm \xi$ with the total decoherence rate $\Gamma_2' = \Gamma_2 + \chi$, as illustrated by the blue curve and the blue open circles in Fig. 6.5(c). In contrast, when the jumping process is fast, $\chi \gg \xi$,

$$S(\omega) \approx \frac{\xi^2/\chi}{(\omega - \omega_0)^2 + [\xi^2/(2\chi)]^2}. \tag{6.6}$$

The qubit absorbs energy only at the frequency ω_0 with $\Gamma_2' = \Gamma_2 + \xi^2/2\chi$, as illustrated by the red curve and the red open triangles in Fig. 6.5(c). The increase

in decoherence rate by $\xi^2/2\chi$ can be related to the excursions of the accumulated phase $\int_0^\tau \xi(t)dt$ (see Publication **X**) for single noise realisations. When χ is comparable with ξ, there is a cross-over region where absorption reduces and the peak broadens due to enhanced decoherence [see the black curve and the black open squares in Fig. 6.5(c)]. This implies that a longitudinally coupled TLS fluctuator is the most poisonous when its internal dynamics occurs approximately at the same frequency as the coupling strength to the host.

6.3 Discussions

If the residual relaxation Γ_1 and decoherence Γ_2 are negligible, the dynamics of the qubit is governed by the Schrödinger equation

$$i\hbar\dot{\hat{\rho}}(t) = \left[\hat{H}_{\rm T}(t), \hat{\rho}(t)\right], \tag{6.7}$$

where

$$\hat{H}_{\rm T}(t) = -\frac{\hbar}{2}\left[\omega_0 + \xi(t)\right]\hat{\sigma}_z + \hbar g\cos(\omega t)\hat{\sigma}_x, \tag{6.8}$$

as given below Eq. (6.4). We can bring the Hamiltonian above into a rotating reference frame with frequency ω and perform a rotating-wave approximation (RWA) to neglect terms oscillating at $\pm(\omega_0+\omega)$,

$$\hat{H}'_{\rm T}(t) = \hat{S}^\dagger(t)\hat{H}_{\rm T}(t)\hat{S}(t) + i\frac{\partial\hat{S}^\dagger(t)}{\partial t}\hat{S}(t) \approx -\frac{1}{2}\left[\Delta + \xi(t)\right]\hat{\sigma}_z + \frac{g}{2}\hat{\sigma}_x, \tag{6.9}$$

with $\hat{S}(t) = \exp(i\omega\hat{\sigma}_z t/2)$ and $\Delta = \omega_0 - \omega$.

The Schrödinger equation Eq. (6.7) is also valid for $\hat{H}'_{\rm T}(t)$ [$\hat{\rho}(t)$ represents the qubit's density matrix in the rotating frame]. In principle we can redefine $\hat{H}'_{\rm T}(t)$ as $\hat{H}_0 + \hat{H}_{\rm Int}(t)$, with the time-independent part $\hat{H}_0 = -(\Delta\hat{\sigma}_z - g\hat{\sigma}_x)/2$ and the time-dependent part $H_{\rm Int}(t) = -\xi(t)\hat{\sigma}_z/2$, and treat the Schrödinger equation in the same way as that in Eqs. (2.15 - 2.20). However, the Markov approximation may be no longer suitable even though the RTN process is Markovian. The time scale characterizing the dynamics of the qubit, τ, is roughly the decoherence time caused by the RTN process. In the slow jumping case $\chi \ll \xi$, $\tau \approx \chi^{-1}$ is comparable to the environment (the RTN signal) correlation time $\tau_r = (2\chi)^{-1}$ (see the Supplementary of Publication **X**). The Markov approximation is not suitable in this case. In the fast jumping case $\chi \gg \xi$, $\tau \approx 2\chi/\xi^2$ is much longer than τ_r, and thus the Markov approximation holds. Therefore the motional averaging may somehow be understood as a transition from non-Markov limit to Markov limit.

7. Summary and Outlook

This thesis contains both theoretical and experimental studies of the decoherence processes and related effects in superconducting quantum circuits. The main results of this thesis can be summarized as follows.

I) In a composite system of two transversely coupled driven qubits, the effects of single-qubit decoherence processes on the entanglement of the two qubits are strongly dependent on the ratio between the inter-qubit coupling strength and the driving amplitude. Steady-state entanglement of the two qubits can be generated in a certain parameter regime.

II) The dynamics of the Autler-Townes effect can be well modeled by a simple three-level Markov master equation. The main differences between the Autler-Townes effect in a superconducting phase qutrit and that in a natural three-level atom are the non-negligible cross-couplings of the microwave tones to the undesired qutrit transitions due to the small anharmonicity of the qutrit. In the non-secular limit, the Autler-Townes splitting is not linearly dependent on the coupling Rabi frequency, due to the decoherence.

III) The single-particle motional averaging effect is experimentally demonstrated in a superconducting transmon qubit by introducing an artificially generated random telegraph noise (RTN) longitudinally coupled to the qubit. The decoherence process caused by the RTN is non-Markovian, and the decoherence rate can not be simply estimated by the noise power of the RTN at zero frequency.

I think the history of developing superconducting quantum qubits is really the history of understanding the decoherence in these circuits. From the first experimental realization of a superconducting qubit [26] to the very recent reports of long decoherence times in superconducting qubits [59, 60], the decoherence times improved by a factor of $\sim 10^4$. Better designs, better fabrications and materials, as well as better engineering of environments for superconducting quantum circuits are all based on better understanding of the decoherence mechanisms. Scaling the

number of qubits up without losing the long decoherence time remains a hot topic in future researchs of superconducting quantum circuits. In another aspect, with only a few qubits (or even just one), simulation of complex many-body or analytically intractable quantum systems, such as the simulation of motional averaging we demonstrated and the simulation of ultra-strong coupling regime [61] which was also briefly mentioned in Publication **X**, can be done. And this is one of the directions I would like to continue in the near future.

A. Average displacement

The exact solutions for Eqs. (2.24) and (2.25) are

$$\langle \hat{a}^\dagger \rangle = c_1 e^{i\omega_0 t} e^{-\gamma t/2} - \frac{2\chi_0 \left[-2\omega_d \cos(\omega_d t) + (\gamma - 2i\omega_0)\sin(\omega_d t)\right]}{\gamma^2 - 4i\gamma\omega_0 - 4\omega_0^2 + 4\omega_d^2} \tag{A.1}$$

and

$$\langle \hat{a} \rangle = c_2 e^{i\omega_0 t} e^{-\gamma t/2} - \frac{2\chi_0 \left[-2\omega_d \cos(\omega_d t) + (\gamma + 2i\omega_0)\sin(\omega_d t)\right]}{\gamma^2 + 4i\gamma\omega_0 - 4\omega_0^2 + 4\omega_d^2}, \tag{A.2}$$

respectively, where $c_{1,2}$ are parameters dependent on the initial state, and the terms with $c_{1,2}$ are called the transient solutions. At time $t \gg \gamma^{-1}$, the transient solutions disappear due to the exponentiall decay $e^{-\gamma t/2}$. Then substituting Eqs. (A.1) and (A.2) into Eq. (2.26), the average displacement takes the form

$$\langle \hat{\Phi} \rangle = -\frac{4\chi_0}{\gamma^4 + 16\left(\omega_0^2 - \omega_d^2\right)^2 + 8\gamma^2\left(\omega_0^2 + \omega_d^2\right)} \sqrt{\frac{\hbar}{2C_\Sigma \omega_0}} A\cos(\omega_d t + \beta), \tag{A.3}$$

where

$$A\cos\beta = -2\omega_d\left(\gamma^2 - 4\omega_0^2 + 4\omega_d^2\right), \tag{A.4}$$

$$A\sin\beta = -\gamma\left(\gamma^2 + 4\omega_0^2 + 4\omega_d^2\right). \tag{A.5}$$

The mean amount of energy absorbed per unit time $I(\omega_d)$ is twice of the mean dissipative function $\bar{F}(\omega_d)$, where

$$F(\omega_d) = \gamma C_\Sigma \left(\frac{d\langle\Phi\rangle}{dt}\right)^2, \tag{A.6}$$

$$\bar{F}(\omega_d) = \frac{1}{2\pi/\omega_d}\int_0^{2\pi/\omega_d} dt F(\omega_d). \tag{A.7}$$

Bibliography

[1] B. D. Josephson. *Phys. Lett.*, **1**:251, 1962.

[2] H. B. G. Casimir. *Proc. Kon. Nederland. Akad. Wetensch. B*, **51**:793, 1948.

[3] C. M. Wilson, G. Johansson, A. Pourkabirian, M. Simoen, J. R. Johansson, T. Duty, F. Nori, and P. Delsing. *Nature*, **479**:376–379, 2011.

[4] M. Schlosshauer. *Rev. Mod. Phys.*, **76**:1267, 2005.

[5] W. H. Zurek. *arXiv:quant-ph/0306072*, 2003.

[6] W. G. Unruh. *Phys. Rev. A*, **51**:992, 1995.

[7] I. L. Chuang, R. Laflamme, P. W. Shor, and W. H. Zurek. *Science*, **270**:1633–1635, 1995.

[8] A. O. Caldeira and A. J. Leggett. *Phys. Rev. Lett.*, **46**:211, 1981.

[9] H.-P. Breuer and F. Petruccione. *The Theory of Open Quantum Systems*. Oxford University Press, New York, 2002.

[10] J. J. Sakurai. *Modern Quantum Mechanics*. Addison-Wesley, Boston, 1994.

[11] M. H. Devoret. *Quantum Fluctuations in Electrical Circuits, Les Houches Session LXIII*. Elsevier Science B. V., Amsterdam, 1995.

[12] L. D. Landau and E. M. Lifshitz. *Mechanics: Volume 1 of Course of Theoretical Physics*. Butterworth-Heinenann, Oxford, 1976.

[13] H. Carmichael. *An Open Systems Approach to Quantum Optics*. Springer-Verlag, Berlin, 1993.

[14] R. R. Puri. *Mathematical Methods of Quantum Optics*. Springer, Berlin, 2001.

[15] C. P. Wen. *IEEE Trans. Microwave Theory Tech.*, **17**:1087, 1969.

[16] D. M. Pozer. *Microwave Engineering*. John Wiley & Sons, New York, 2005.

[17] R. N. Simons. *Coplanar Waveguide Circuits, Components, and Systems*. John Wiley & Sons, New York, 2001.

[18] M. Ohring. *Materials Science of Thin Films Deposition and Structure*. Academic Press, San Diego, 2002.

[19] P. Rai-Choudhury. *Handbook of Microlithography, Micromachining, and Microfabrication Volume 1: Microlithography*. SPIE, Washington, 1997.

[20] Showa Denko K. K., Tokyo. *ESPACER 300 Technical Data Sheet*, 2007.

[21] MicroChem Corp., Newton. *NANO^{TM} PMMA and Copolymer*, 2001.

[22] L. Frunzio, A. Wallraff, D. Schuster, J. Majer, and R. Schoelkopf. *IEEE Trans. Appl. Supercond.*, **15**:860, 2005.

[23] K. K. Likharev. *Dynamics of Josephson Junctions and Circuits*. OPA Ltd., Amsterdam, 1986.

[24] M. Tinkham. *Introduction to Superconductivity*. McGraw-Hill, New York, 1996.

[25] M. H. Devoret and J. M. Martinis. *Quantum Inf. Proc.*, **3**:163, 2004.

[26] Y. Nakamura, Y. A. Pashkin, and J. S. Tsai. *Nature*, **398**:786–788, 1999.

[27] J. M. Martinis, S. Nam, J. Aumentado, and K. M. Lang. *Phys. Rev. B*, **67**:094510, 2003.

[28] M. A. Nielsen and I. L. Chuang. *Quantum Computation and Quantum Information*. Cambridge University Press, Cambridge, 2000.

[29] D. Vion, A. Aassime, A. Cottet, P. Joyez, H. Pothier, C. Urbina, D. Esteve, and M. H. Devoret. *Science*, **296**:886–889, 2002.

[30] J. Koch, T. M. Yu, J. Gambetta, A. A. Houck, D. I. Schuster, J. Majer, A. Blais, M. H. Devoret, S. M. Girvin, and R. J. Schoelkopf. *Phys. Rev. A*, **76**:042319, 2007.

[31] A. Blais, R.-S. Huang, A. Wallraff, S. M. Girvin, and R. J. Schoelkopf. *Phys. Rev. A*, **69**:062320, 2004.

[32] A. Wallraff, D. I. Schuster, A. Blais, L. Frunzio, R.-S. Huang, J. Majer, S. Kumar, S. M. Girvin, and R. J. Schoelkopf. *Nature*, **431**:162–167, 2004.

[33] A. Blais, J. Gambetta, A. Wallraff, D. I. Schuster, S. M. Girvin, M. H. Devoret, and R. J. Schoelkopf. *Phys. Rev. A*, **75**:032329, 2007.

[34] W. P. Schleich. *Quantum Optics in Phase Space*. Wiley-VCH, Berlin, 2001.

[35] T. Niemczyk, F. Deppe, H. Huebl, E. P. Menzel, F. Hocke, M. J. Schwarz, J. J. Carcia-Ripoll, D. Zueco, T. Hümmer, E. Solano, A. Marx, and R. Gross. *Nature Phys.*, **6**:772–776, 2010.

[36] P. Forn-Díaz, J. Lisenfeld, D. Marcos, J. J. García-Ripoll, E. Solano, C. J. P. M. Harmans, and J. E. Mooij. *Phys. Rev. Lett.*, **105**:237001, 2010.

[37] C. Cohen-Tannoudji, J. Dupont-Roc, and G. Grynberg. *Atom-Photon Interactions*. Wiley, New York, 1992.

[38] J. M. Fink, M. Göppl, M. Baur, R. Bianchetti, P. J. Leek, A. Blais, and A. Wallraff. *Nature*, **454**:315–318, 2008.

[39] A. Wallraff, D. I. Schuster, A. Blais, L. Frunzio, J. Majer, M. H. Devoret, S. M. Girvin, and R. J. Schoelkopf. *Phys. Rev. Lett.*, **95**:060501, 2005.

[40] O. Astafiev, Yu. A. Pashkin, Y. Nakamura, T. Yamamoto, and J. S. Tsai. *Phys. Rev. Lett.*, **93**:267007, 2004.

[41] A. Shnirman, G. Schön, I. Martin, and Y. Makhlin. *Phys. Rev. Lett.*, **94**:127002, 2005.

[42] R. W. Simmonds, K. M. Lang, D. A. Hite, S. Nam, D. P. Pappas, and J. M. Martinis. *Phys. Rev. Lett.*, **93**:077003, 2004.

[43] K. B. Cooper, M. Steffen, R. McDermott, R. W. Simmonds, S. Oh, D. A. Hite, D. P. Pappas, and J. M. Martinis. *Phys. Rev. Lett.*, **93**:180401, 2004.

[44] R. F. Werner. *Phys. Rev. A*, **40**:4277, 1989.

[45] L. Amico, R. Fazio, A. Osterloh, and V. Vedral. *Rev. Mod. Phys.*, **80**:517, 2008.

[46] T. Yu and J. H. Eberly. *Phys. Rev. Lett.*, **93**:140404, 2004.

[47] T. Yu and J. H. Eberly. *Phys. Rev. Lett.*, **97**:140403, 2006.

[48] M. P. Almeida, F. de Melo, M. Hor-Meyll, A. Salles, S. P. Walborn, P. H. Souto Ribeiro, and L. Davidovich. *Science*, **316**:579–582, 2007.

[49] W. K. Wootters. *Phys. Rev. Lett.*, **80**:2245, 1998.

[50] T. Yu and J. H. Eberly. *Quantum Inf. Comput.*, **7**:459, 2007.

[51] Y. Makhlin. *Quantum Inf. Proc.*, **1**:243, 2002.

[52] J. Zhang, J. Vala, S. Sastry, and K. B. Whaley. *Phys. Rev. A*, **67**:042313, 2003.

[53] M. O. Scully and M. S. Zubairy. *Quantum Optics*. Cambridge University Press, Cambridge, 1997.

[54] A. Abragam. *Principles of Nuclear Magnetism*. Oxford University Press, New York, 1961.

[55] T. Kohmoto, Y. Fukuda, M. Kunitomo, K. Ishikawa, M. Tanigawa, K. Ebina, and M. Kaburagi. *Phys. Rev. B*, **49**:15352, 1994.

[56] Y. Sagi, R. Pugatch, I. Almog, and N. Davidson. *Phys. Rev. Lett.*, **104**:253003, 2010.

[57] Y. Yamamoto. *Fundamentals of Noise Processes*. EE/AP 248 online lecture notes, Stanford University.

[58] M. I. Dykman, M. Khasin, J. Portman, and S. W. Shaw. *Phys. Rev. Lett.*, **105**:230601, 2010.

[59] J. Bylander, S. Gustavsson, F. Yan, F. Yoshihara, K. Harrabi, G. Fitch, D. G. Cory, Y. Nakamura, J.-S. Tsai, and W. D. Oliver. *Nature Phys.*, **7**:565–570, 2011.

[60] H. Paik, D. I. Schuster, L. S. Bishop, G. Kirchmair, G. Catelani, A. P. Sears, B. R. Johnson, M. J. Reagor, L. Frunzio, L. I. Glazman, S. M. Girvin, M. H. Devoret, and R. J. Schoelkopf. *Phys. Rev. Lett.*, **107**:240501, 2011.

[61] D. Ballester, G. Romero, J. J. García-Ripoll, F. Deppe, and E. Solano. *Phys. Rev. X*, **2**:021007, 2012.

Aalto-DD 102/2012

ISBN 978-952-60-4729-4
ISBN 978-952-60-4730-0 (pdf)
ISSN-L 1799-4934
ISSN 1799-4934
ISSN 1799-4942 (pdf)

Aalto University
School of Science
O.V. Lounasmaa Laboratory
www.aalto.fi

BUSINESS +
ECONOMY

ART +
DESIGN +
ARCHITECTURE

SCIENCE +
TECHNOLOGY

CROSSOVER

DOCTORAL
DISSERTATIONS